Università di Pisa

Facoltà di Scienze Matematiche Fisiche e Naturali

Corso di Laurea Specialistica in Fisica Applicata

Anno Accademico 2004/2005

Tesi di Laurea Specialistica

Development and assessment of tools for quantitative dynamic contrast enhanced MRI of bone metastases from breast and prostate cancer

Candidato

Christian Bracco

Relatori

Prof. Alberto Del Guerra

Prof. Mario Ferraro

Marge: Homer! There's someone here who can help you...
Homer: Is it Batman?
Marge: No, he's a scientist.
Homer: Batman's a scientist?!
Marge: It's not Batman!"

Acknowledgments

This work was carried out at the unit of radiology of the IRCC (Institute for Cancer Research and Treatment) in Turin. I wish to express sincere gratitude to those who in different ways have supported me in this work and have made this thesis a reality. My special thanks go to:

Dr. Alberto Bert, thank you for many fruitful and interesting discussions covering many topics during the months when we shared an office. Thank you for all your help during the collection and analysis of the basic data and during the work of this thesis.

Professor Mario Ferraro, who has always been there with interest, support and time for discussion.

Professor Mark Mandelkern, who gave me important advice and support on this work. Thank you for making possible a connection between the IRCC of Turin and the Physics Department of Pisa.

Daniele Regge, M.D. who in the busy and demanding clinical activities of Radiology department always manages to defend the important position of research linked to clinical issue.

All the personnel at the unit of Radiology who was so unlucky to meet me. Special thanks to Dr. Filippo Russo and Dr. Laura Martincich who provided the first patients, thanks to Dr. Patrizia Della Monica who managed the time table of the experiments and gave me some indications on the surface coils, thanks to the MRI technologists who are always interested in new applications.

My mother and my father who taught me to never give up, to be curious, to think positive, but also to show respect and understanding.

All my friends at the University of Pisa, in particular the people of Medical Physics group, thanks for your hospitality and the great time I had with you.

Last but not least, special thanks to Professor Alberto Del Guerra, my tutor at the University of Pisa, who gave me the great opportunity to spend some months at the University of California Irvine, where I met people who made enormously and greatly change my life. Thanks again.

Table of Contents

Abstract

The microenvironment of solid human tumors is characterized by heterogeneity in oxygenation and by proliferation of a network of blood vessels that provides oxygen and nutrients and removes waste products. The capability of a tumor to metastasize is linked to the well known hyper permeability of tumor vessels; in fact angiogenic primary tumors possess a large number of micro-vessels through which the metastasizing cells are shed into the blood stream. Pioneering studies performed by Folkman in 1971 proposed an insightful anticancer therapy by starvation of blood supply, Folkman's intuition that tumor growth and metastasis strictly depend on angiogenesis led to the idea that blocking tumor nourishment could be one of the ways to avoid its spread. Many imaging strategies have been used to determine angiogenesis in vivo, among them Dynamic Contrast Enhanced MRI (DCE-MRI) which provides a powerful tool for the rapid evaluation of the acute pharmacodynamic effect of the most recent agents in clinical trials, most notably in the case of mechanisms that affect tumor perfusion. One of the attractives of dynamic post contrast imaging is the insight it offers into the distribution kinetics of contrast agent in the tissue. These quantities are generally derived from simple models of the tissue as a compartmentalized system (usually a plasma-interstitial two-compartments model is used), using a kinetic analysis originally developed for use with nuclear medicine tracers. In this study a three parameters model has been used in order to describe the transport of tracer in the tissues. The first one takes into account the plasma volume in the voxel or in the region of interest being examined, the second is related to the amount of tracer that enters the EES and the last one determines the washout rate from EES back into the blood plasma. An artery input function (AIF), namely the concentration of contrast in the plasma, is provided as well. In order to obtain these parameters it is necessary to perform the fit of the chosen model on the concentration-curves vs time. It is possible to correlate the contrast agent concentration with the difference of relaxation rate (the inverse of longitudinal relaxation time); this way the concentration-curves can be achieved by means of T_1-weighted images. In this work, an acquisition protocol has been optimized in order to provide the images from which extracting the data related to the tumor perfusion. Post processing tools, which carry out the fitting, the smoothing, and, the registration, have been developed and tested, as well. These tools can provide

the oncologists and radiologists a way to perform reproducible and quantitative estimation of the therapy-course.

Introduction

The skeleton is the most frequently affected organ in metastatic breast and prostate cancer. The primary aim of bone metastasis treatment is to achieve optimal control of patient pain and to reduce pathological complications. The usual treatment for bone metastases is a proper combination of chemotherapy, endocrine therapy, radiotherapy and surgery.

Current methods of bone-metastasis assessment do not accurately predict pathological response during therapy. Bone scintigraphy and traditional X-ray characterize the response to therapy indirectly, are relatively nonspecific and, detect changes after a relatively long period from the beginning of treatment. More sensitive diagnostic tools are necessary in order to identify positive or negative responses shortly after beginning therapy. Contrast-enhanced magnetic resonance imaging (MRI), particularly DCE-MRI, see section 1.2 on page 10, is the method of choice for accurately evaluating the degree of tumor response to the applied therapy in soft-tissue cancers and sarcomas of bone. DCE-MRI is able to identify early signal modifications in bone metastases after biphosphonate treatment, these modifications, related to bone tissue repair, are strongly correlated with patient prognosis [1].

A large range of technique have been applied to the analysis of signal enhancement curves observed in DCE-MRI which ranges from simple visual inspection to complex quantification using applications of pharmacokinetic models. Many analysis techniques are based on measurements taken from user defined region of interest (ROI). This has the advantage of ease off use but also has the disadvantage in that it produces a wide degree of variability and potential intra observer errors into the technique. More importantly it is incapable of identifying or quantifying significant heterogeneity within the tumor microvascular which may occur within the ROI. Inappropriate selection of the ROI so that it includes both enhancing and necrotic or non enhancing components of tumor would give rise to misleading interpretation. These shortcomings can be addressed by the production of calculated parametric images which allow pixelwise analysis of the calculated microvascular components. This pixelwise analysis deals with tumor heterogeneity and potentially provides a far wider range of information concerning tumor behavior than is available from region of interest analysis. A broad range of approaches have been taken to asses the properties of enhancement curves

in various tumors. Most of these techniques are designed to deal with baseline variations in signal intensity and with the inherent differences in signal intensity that would be observed due to changes in tuning and scaling factors between scanners or even between sessions on the same scanner. Heywang and co-workers (1989) proposed a classification scheme for breast lesions using normalized signal intensities (NU) where lesions beyond the threshold of 300 were classified as malignant, $250 - 300$ as borderline and below 250 NU as non malignant, Kaiser et al. (1989) normalized the signal enhancement using the intensity of the lesion before contrast injection and defined malignant lesions as those showing a signal enhancement of at least 100% during the first minute. Others workers (Boetes et al. 1994; Gilles et al. 1994) have identified the presence of very early enhancement in the tumor after the arrival of the arterial bolus as an indicator of malignancy.

These studies illustrate the potential problems in the use of signal enhancement curves to study malignant vasculature. Firstly, the signal intensity changes are non specific and will vary according to a wide range of scanner parameters. Because of non linear relationship between contrast concentration and signal intensity changes and the wide variation in baseline T_1, see section 2.2 on page 23, values and signal intensity seen in the tissues being studied, attempts to calibrate or produce standard images which could be used in multiple sites have not been successful. Subjective enhancement curve analysis must therefore include some form of curve normalization to account for these variation which are principally seen as difference in the amplitude of the enhancement curve. Secondly, the enhancement curves will contain important information not only in terms of amplitude but also in terms of time of arrival and curve slope. The choice of normalization technique and of the most representative curve shaped parameters is difficult and has led to the development of many semi quantitative or descriptive systems. Different methods have been applied in different application and in different tissues. Despite these shortcoming semiquantitative curve shape analysis techniques can be extremely valuable, particularly in clinical application for the grading or classification of tumors. This reflect the fact that difference in tumor vasculature between benign and malignant tumors are large and may be demonstrated by relatively crude analysis techniques. Despite their clear clinical utility the shortcoming of these semi quantitative techniques have led many workers to develop more robust quantitative approaches to analysis. There are several reasons why more quantitative approaches may be beneficial. Firstly, the ability to produce measurements which reflected the physiological anatomical structure of the tumor microvasculature and which are truly independent of scanner acquisition and tumor type is highly attractive when compared to the use of a range of tissue or scanner specific semi quantitative methods. Secondly, the development of precise and reproducible quantitative measures is highly desirable for use in longitudinal or multi centre studies. This is of particular importance in clinical trials of new therapeutic agents where the ability to test the hypoth-

esis that an agent affects tumor microvasculature will depend entirely on the accuracy and reproducibility of measure used. Thirdly, it must be appreciated that signal enhancement curves are a crude indicator of the contrast distribution mechanisms that are occurring within the voxel. Even a small imaging voxel is large by biological standards and may contain varied proportions of blood vessels, cells and extracellular extravascular (EES) space. A signal enhancement curve may therefore represent contrast which is principally in blood vessels, contrast which has principally leaked into the EES or any combination of these. Contrast enhancement curves cannot therefore differentiate between voxels which contain few vessels but have rapid leakage of contrast medium into EES and voxels in which there is little leakage but a large vascular fraction. Fourthly, simple analyses of contrast enhancement curves are unable to compensate for variations in the contrast delivery to the tumor, which might occur due to poor injection technique, anatomical variations or abnormal physiological features in the individual patients such as poor cardiovascular function. Since these technique are widely used in cancer patients where venous access can be difficult and cardiovascular and renal functions are commonly compromised this can introduce significant variation into the results of quantitative analysis techniques.

The optimal analysis of DCE-MRI data would be designed to identify specific quantitative physiologic parameters which describe the tissue microvasculature being observed. This type of analysis requires the application of a quantitative mathematical model which describes the pharmacokinetics of the contrast agent. In order to apply pharmacokinetic models of contrast distribution to imaging based data the first essential step is to use the signal changes observed in the dynamic acquisition to calculate quantitative parametric images of contrast concentration at each time point. Since the relationship between signal intensity and contrast concentration may be non linear this adds an additional complication and often requires the measurement of pre contrast T_1 values for each of the voxels to be studied. Using these quantitative T_1 images together with the observed signal change it is possible to transform each of the images within the dynamic time course series to a parametric image of contrast concentration. These contrast-concentration vs time-course curves, for individual voxels, are then used as the substrate for pharmacokinetic models.

DCE-MRI has clearly established itself as a valuable imaging method, the majority of results to date have come from a small number of dedicated groups who are willing and able to expend considerable resources on coping with the lack of validated software for DCE-MRI image registration and analysis. Wider use of this imaging method in clinical trials and studies will depend on making such software available and refining it to function efficiently in the clinic.

This work deals with the development and assessment of tools for non invasive and quantitative analysis of tumor perfusion, more in particular, it is examined the perfusion of bone metastasis from prostate, treated with difosfonate and chemoterapy, and breast cancer treated with endocrine therapy. Disease

with bone metastasis demonstrates a slow clinical course and is associated with prolonged survival compared to disease with liver or lung metastasis. The availability of effective anti-endocrine agents makes endocrine therapy associated with biphosphonate treatment a valuable anticancer treatment in this illness (breast cancer metastases). This combination therapy is less aggressive than alternative chemotherapies, with fewer and less severe complications. DCE-MRI is planned before the beginning of therapy (baseline), between the 15th and the 21th day of the treatment (post 1st cycle), between the 30th and the 42th day of therapy (post 2nd cycle), and after the 4th month of therapy. Multislice CT imaging is carried out together with the baseline and last DCE-MRI, as indicated clinically.

The tools consist of scanning protocol and, imaging processing dedicated to computing parametric maps. The scanning protocol is composed of a variable flip angle, see section 3.3 on page 45, necessary to measure the T_1 pre-contrast of tissues; it is also included a 3D dynamic GRE, see section 2.5.5 on page 34, which is used in order to acquire the time-course of contrast agent in the districts being imaged. Several tests were performed in order to optimize parameters of the sequences in scanning protocol, these tests were carried out on a phantom and on several volunteers. Simultaneously, the code required to compute the T_1 maps, smooth and coregister the images and, perform the fitting is developed and tested on synthetic images and on phantom as well. Some statistical analyses are carried out on the data collected from the same patient over a period of four months.

This thesis is composed of two main parts, in the first one (first and second chapter), the biological bases of angiogenesis, the mathematical bases of the compartmental model and, the essential physical bases of MRI, the imaging method used to acquire the images, are provided; the second part (third and fourth chapter) shows the method used in order to build the contrast concentration time course curves and the way to reach and analyze the parametric maps.

Chapter 1

Angiogenesis and compartmental model

1.1 Angiogenesis and tumor vasculature

Angiogenesis is a crucial mechanism required for a number of physiological and pathological events [2]. In physiological conditions, angiogenesis is a highly regulated phenomenon. Normally occurs during embryonic development, wound healing, and the menstruation cycle. Unregulated angiogenesis takes place in pathological conditions, such as psoriasis, diabetic retinopathy and cancer.

In physiologic conditions, cells are located within 100 and 200 μm from blood vessels, their source of oxygen. When a multicellular organism is growing, cells induce angiogenesis and vasculogenesis in order to recruit new blood supply. In a pathological condition such as cancer, angiogenesis is necessary for tumor survival and proliferation. The microenvironment of solid human tumors is characterized by heterogeneity in oxygenation and by proliferation of a network of blood vessels that penetrates into tumors supplies oxygen and nutrients and removes waste products. Formation of solid tumors requires coordination of angiogenesis with continued tumor cell proliferation; however, despite such neo-vascularization, hypoxia is persistent and frequently found in tumors at the time of diagnosis. Hypoxia arises early in the process of tumor development because rapidly proliferating tumor cells outgrow the capacity of the host vasculature. Tumors with low oxygenation have a poor prognosis, and strong evidence suggests that this is because of the effects of hypoxia on malignant progression, angiogenesis, metastasis, and therapy resistance. Tumor cells located more than 100 μm away from blood vessels become hypoxic, some clones will survive by activating an angiogenic pathway. If new blood vessels do not form, tumor clones will be confined within $1 - 1.5$ mm diameter. Such clones remain dormant from months to years before they switch to an angiogenic phenotype. Vascular cooption is confined only in the tumor periphery and gradual tumor expansion causes a progressive cen-

tral hypoxia. Hypoxia induces the expression of pro-angiogenic factors through hypoxia-inducible factor-α, and if pro-angiogenic factors are in excess of anti-angiogenic factors, it may lead to the switch to an angiogenic phenotype. The presence of viable hypoxic cells is likely a reflection of the development of hypoxia tolerance resulting from modulation of cell death in the microenvironment. This acquired phenotype has been explained on the basis of clonal selection. The hypoxic microenvironment selects cells capable of surviving in the absence of normal oxygen availability. However, the persistence and frequency of hypoxia in solid tumors raise a second potential explanation. It has also been suggested that stable micro-regions of hypoxia may play a positive role in tumor growth. Although hypoxia inhibits cell proliferation and eventually cell death, hypoxia also provides angiogenic and metastatic signals, thus allowing prolonged survival in the absence of oxygen and generation of a persistent angiogenic signal.

The first interest in angiogenesis related to cancer was in 1968 [3], when it was first highlighted that tumor secretes a diffusible substance that stimulates angiogenesis. Since then, several investigators studied the different pro-angiogenic factors that tumor cells diffuse when the mass has reached the limited size of the early tumor. Pioneering studies performed by Folkman in 1971 [4] proposed an insightful anticancer therapy by starvation of blood supply, Folkman's intuition that tumor growth and metastasis strictly depend on angiogenesis led to the idea that blocking tumor nourishment could be one of the ways to avoid its spread.

Several sequential steps can be highlighted during tumor angiogenesis. In mature (non-growing) capillaries, the vessel wall is composed of an endothelial cell lining, a basement membrane, and a layer of cells called pericytes, which partially surround the endothelium. The pericytes are contained within the same basement membrane as the endothelial cells and occasionally make direct contact with them. Angiogenic factors produced by tumoral cells bind to endothelial cell receptors and initiate the sequence of angiogenesis. When the endothelial cells are stimulated to grow, they secrete proteases, heparanase, and other digestive enzymes that digest the basement membrane surrounding the vessel.

Degradation of basement membrane and the extracellular matrix surrounding pre-existing capillaries, usually post-capillary venules, is a mechanism allowed by matrix metalloproteinases (MMPs), a family of metallo-endopeptidase secreted by the tumor cells and the supporting cells. The dissolution of extracellular matrix also allows the release of pro-angiogenic factors from the matrix. The junctions between endothelial cells become altered, cell projections pass through the space created, and the newly formed sprout grows toward the source of the stimulus. Endothelial cells invade the matrix and begin to migrate and proliferate into the tumor mass. In this location, newly formed endothelial cells organize into hollow tubes (canalization) and create new basement membrane for vascular stability. Fused blood vessels newly established form the blood flow within the tumor.

The capability of a tumor to successfully metastasize is linked to angiogenesis

[5], in fact angiogenic primary tumors possess a large number and size of microvessels through which the metastasizing cells are shed into the blood stream; with increased angiogenesis the number of metastasizing cells can increase 100-fold or more. The well-recognized hyper-permeability of tumor vessels, tied to angiogenesis, may also contribute to the transendothelial escape of tumor cells; new, proliferating capillaries have fragmented basement membranes that partially account for this hyperpermeability. Having entered the circulation, the cells must survive the journey, escape immune surveillance, penetrate (or grow from within) the microvessels of the target organ, and again induce angiogenesis in the target in order to grow beyond 2 mm in diameter. It is noteworthy that angiogenesis may not be sufficient, in itself, for metastases to occur. However, the inhibition of angiogenesis prevents the growth of tumor cells at both the primary and secondary sites and thereby can prevent the emergence of metastases.

Being a limiting factor for both tumor growth and metastases, it has been assumed that angiogenesis correlates with tumor aggressiveness. Indeed, this assumption has been supported in clinical series investigating a variety of tumor types. Histologic assays of angiogenesis based on the microvascular density (MVD), the number of endothelial clusters in a high-power microscopic field, in randomly selected human breast cancers showed that MVD correlated with the presence of metastases at time of diagnosis and with decreased patient survival times. MVD is widely accepted as a measurable surrogate of the angiogenesis process.

The structure of solid tumors is fundamentally chaotic [6], in contrast to the elegant and ordered anatomical design of normal tissues and organs. Tumor microcirculation differs profoundly from that of normal organs in three ways:

- Flow characteristics and, sometimes, the blood volume of the microvasculature;
- Microvascular permeability;
- For many malignant tumors, in the increased fractional volume of Extracellular Extravascular Space (EES).

The microvasculature is now known to be aberrant in many malignant tumors and in leukemic bone marrow, because of tumor-derived factors that stimulate the endothelial cells to form new small vessels (angiogenesis) and affect the maturation of these vessels (vasculogenesis). The network of blood vessels in many solid tumors has been shown to deviate markedly from normal hierarchical branching patterns and to contain gaps in which tumor cells lack close contact with perfusing vessels. This phenomenon has been shown in a variety of solid tumors to lead to blood flow that is both spatially and temporally more heterogeneous than the efficient, uniform perfusion of normal organs and tissues. In addition to these abnormalities, tumors often differ markedly from the surrounding organ in

the permeability (more properly, permeability × surface area product) of their capillaries. This altered permeability is important in itself, because it changes the rules governing the transfer of compounds between blood and tumor tissue. There is a third abnormality, which specifically affects the trapping and clearance of agents in tumors. This is the marked alteration in relative volumes of major tissue compartments (vascular, intracellular, and extravascular-extracellular), with expansion of the EES distribution volume. In cases of tissue injury or pathology, the fractional EES volume, v_e, may increase significantly.

1.2 Imaging angiogenesis

The imaging strategies that have been used to determine angiogenesis in vivo are Dynamic Contrast Enhanced Magnetic Resonance Imaging (DCE-MRI), Positron Emission Tomography (PET) and Computerized Tomography (CT) [7].

DCE-MRI can monitor the effectiveness of a variety of treatments, including chemotherapy, hormonal manipulation, and radiotherapy, and novel therapeutic approaches, including antiangiogenic drugs; DCE-MRI provides a powerful tool for the rapid evaluation of the acute pharmacodynamic effect of the novel agents in clinical trials, most notably in the case of mechanisms that affect tumor perfusion. Evidence is mounting that DCE-MRI measurements correlate with immunohistochemical surrogates of tumor angiogenesis.

In DCE-MRI, imaging is performed at the same time as contrast administration, and it has been used in a large number of studies to examine tumor vasculature. It is a non invasive technique that yields parameters related to tissue perfusion (T_2 methods 2.2 on page 23) and permeability (T_1 methods 2.2 on page 23). The paramagnetic contrast agent gadopentetate dimeglumine (Gd-DTPA) is injected as a rapid intra venous bolus and, as it passes through tissues, it diffuses out of the blood vessels into the EES. The signal intensity on T_1-weighted images increases as the concentration of Gd-DTPA in the extracellular space increases. These changes in signal intensity are recorded by serial images acquired before, during, and after the injection. Relative changes in semiquantitative parameters, such as the maximum gradient of the signal-intensity-time curve, the maximum increase in signal intensity normalized to baseline signal intensity (enhancement), and the area under the initial part of the curve, can be examined and are indirectly related to changes in the physiologic end points of interest: tissue perfusion, vascular permeability, and vessel surface area.

PET is a sensitive and quantitative technique that can be used to monitor the pharmacokinetics and pharmacodynamics of drugs when radio labeled with positron-emitting radioisotopes. PET has been applied to a wide range of drugs to demonstrate activity in vivo including standard chemotherapy and antiangiogenic and antivascular therapy. Although PET finds such a wide application in several studies, this technique uses ionizing radiation, limiting the number of studies that

can be performed on the same patient to assess the course of a therapy. Although MRI is less quantitative than PET, the limitation concerning ionizing radiation does not apply to MRI.

Dynamic or functional CT can be readily incorporated into routine conventional CT examinations, and the physiological parameters obtained can provide an in vivo marker of angiogenesis in tumors. Using this technique , it is possible to determine absolute values for tissue perfusion, relative blood volume, capillary permeability, and leakage. These parameters provide physiological correlates for the microscopic changes that occur with tumor angiogenesis. Tumor angiogenesis is characterized morphologically by increased numbers of small blood vessels. These microvessels are too small to image directly, but their increased density translates in vivo to increased tumor perfusion and blood volume. Dynamic CT has been used by various investigators to evaluate tumor microvessels density. Dynamic CT is simple, widely available and reproducible. Quantification is simpler than for MRI, as the relationship between signal and contrast concentration is much more linear than that seen with MRI, although the sensitivity is less. The problem is that early clinical studies of antiangiogenic compounds require multiple imaging assessments of the tumor. As contrast-enhanced dynamic CT necessarily uses ionizing radiation, there is a limit to the number of studies that can be performed in any one patient. However, the imaging techniques discussed above have their advantages and disadvantages. PET is not a specific technique and problems can occur due to antiangiogenesis drug-induced uncoupling of tumor perfusion and other aspects of tumor physiology, furthermore, PET still lacks sufficient availability to be considered a viable clinical approach for routine application. CT involves exposure to ionizing radiation and has not yet demonstrated a reduction in tumor perfusion by antiangiogenic therapies. DCE-MRI has been used in the early clinical trial evaluation of a number of antiangiogenic and antivascular compounds. Data have shown that the techniques used are reproducible and, to a significant extent, valid.

One of the attractions of dynamic post contrast imaging is the potential insight it offers into contrast agent distribution kinetics in the tissue [8]. These quantities are generally derived from simple models of the tissue as a compartmentalized system (usually a plasma-interstitial two-compartments model is used), using of kinetic analysis strategies originally developed for use with nuclear medicine tracers.

1.3 Theoretical basis of the model

Low molecular weight contrast media available for clinical MRI studies, such as Gd-DTPA, transfer between the blood pool and the EES of the tissue of the tumor at a rate determined by the blood flow to the tissue, the permeability of the blood vessel walls and, the surface area of the perfusing vessel. The contrast

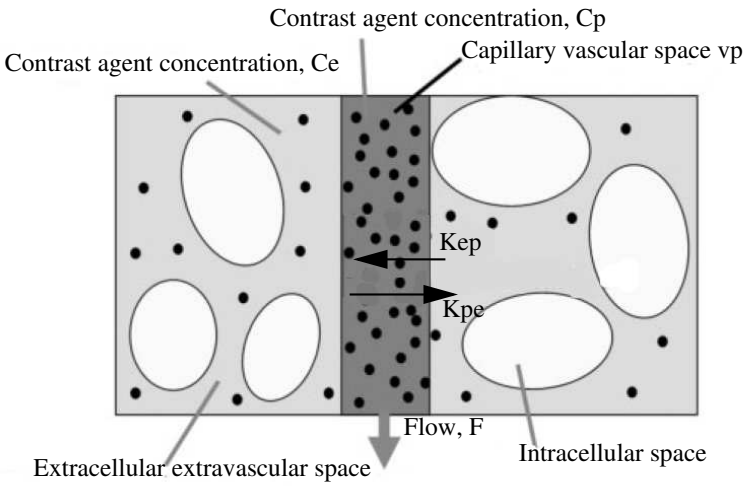

Figure 1.1: Major compartments and functional variables involved in the distribution of contrast agent tracer in tissue.

agent does not cross cell membranes and its volume of distribution is therefore effectively the EES. In the presence of well-perfused and leaky vessels contrast medium immediately begins to pass into the EES. Over a period lasting many hours, the contrast agent is removed from the blood stream by renal excretion and, it therefore washes out of the EES. A compartmental model can be used to describe the transport of Gd-DTPA in tissue vascular and interstitial spaces as a function of time [9, 10, 11], which allows the determination of tracer concentration in tissue. The model basically consists of two compartments: a plasma compartment and a EES compartment, see figure 1.1. The EES compartment is actually the leakage space within the interstitial space of the selected tissue region. The transport of tracer from the plasma compartment into the extravascular compartment can be expressed as:

$$\frac{dC_e(t)}{dt} = k_{pe}C_p(t) - k_{ep}C_e(t) \tag{1.1}$$

where $C_p(t)$ and $C_e(t)$ are the tracer concentration in the plasma and EES compartments, respectively, in units of mM, k_{ep} and k_{pe} are the transport constants related to the leakage space, in units of min^{-1}.

Eqn. 1.1 is a simple *first order* differential equation for $C_e(t)$, next it is explained how to find a solution. Let $C_e(t) = A(t)e^{-k_{ep}t}$ be a test function, by substituting this test function in Eqn. 1.1 we obtain

$$\begin{aligned} \frac{dA(t)}{dt}e^{-k_{ep}t} - k_{ep}A(t)e^{-k_{ep}t} &= k_{pe}C_p(t) - k_{ep}A(t)e^{-k_{ep}t} \\ \frac{dA(t)}{dt} &= k_{pe}C_p(t)e^{k_{ep}t} \end{aligned} \tag{1.2}$$

and, by integrating Eqn. 1.2 on the preceding page

$$C_e(t) = k_{pe} \int_0^t C_p(\tau) e^{-k_{ep}(t-\tau)} d\tau \tag{1.3}$$

The total concentration in a selected voxel in tissue, $C_T(t)$, comes from the contributions of both plasma and extravascular compartments,

$$C_T(t) = v_p C_p(t) + v_e C_e(t) \tag{1.4}$$

where v_p is the plasma volume fraction and v_e is the leakage space fraction in the voxel, no units. By substituting Eqn. 1.3 in Eqn. 1.4 we obtain:

$$C_T(t) = v_p C_p(t) + K^{\text{trans}} \int_0^t C_p(\tau) e^{-k_{ep}(t-\tau)} d\tau \tag{1.5}$$

where we introduced the parameter K^{trans} defined as the product $v_e k_{pe}$. Thus K^{trans} determines the amplitude of the initial response (the amount of tracers that enters the EES), and k_{ep} determines the washout rate from EES back into the blood plasma.

The concentration of contrast agent in the plasma $C_p(t)$ (the *arterial input function* AIF) is assumed to follow a linear increase phase after injection to the maximum value, then follow a biexponential decay with two rate constant [12]. The following equation is used to describe the observed biexponential decay:

$$C_p(t) = Ae^{-m_1 t} + Be^{-m_2 t} \tag{1.6}$$

where A and m_1 are respectively the amplitude and rate constants of the fast exponential decay (contrast leakage into the interstitium), and B and m_2 are respectively the amplitude and rate constants of the slow exponential decay i.e. $m_1 \ll m_2$. This function is not the only one curve utilized to describe the contrast agent concentration in the blood, depending on the functional parameters being examined one can make more or less complicated the function approximating $C_p(t)$ [12].

The influence of each physiological parameter on the curves is best understood by taking a look at the figures 1.2 to 1.4 on pages 14–15. All the curves are obtained by means of the Eqn. 1.5, the $C_p(t)$ is measured on a patient, for each figure two parameters are kept fixed while one parameter is free to vary in a range of physical values. The initial slope of the curves is principally influenced by the K^{trans} parameter, the higher its value the higher the initial slope of the curve; v_p value makes the curves look like the C_p, whereas k_{ep} influences the early curvature and peak, the wash out first starts wherever this value is high. The model just examined is not the only one available to describe the transport of Gadolinium between the compartment, more complicated (four parameters) or simpler (just two parameters) model can be used, Buckley [11] shows advantages

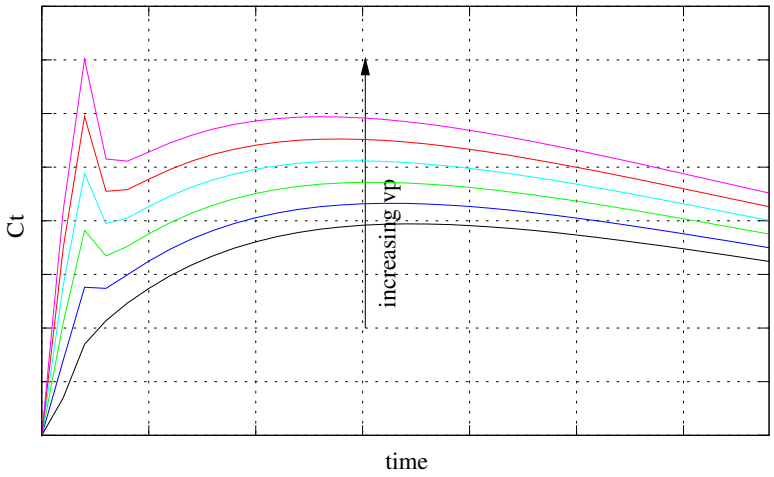

Figure 1.2: Simulated curves related to the gadolinium transport between the compartments. The influence of v_p parameters is shown.

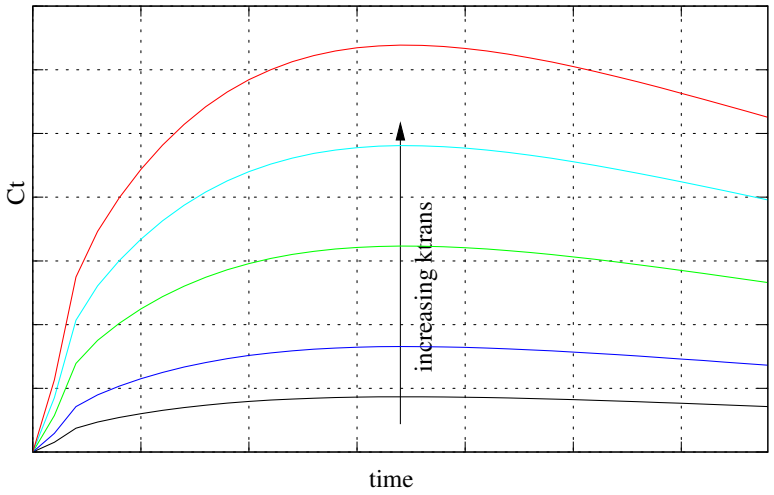

Figure 1.3: Simulated curves related to the gadolinium transport between the compartments. The influence of K^{trans} parameters is shown.

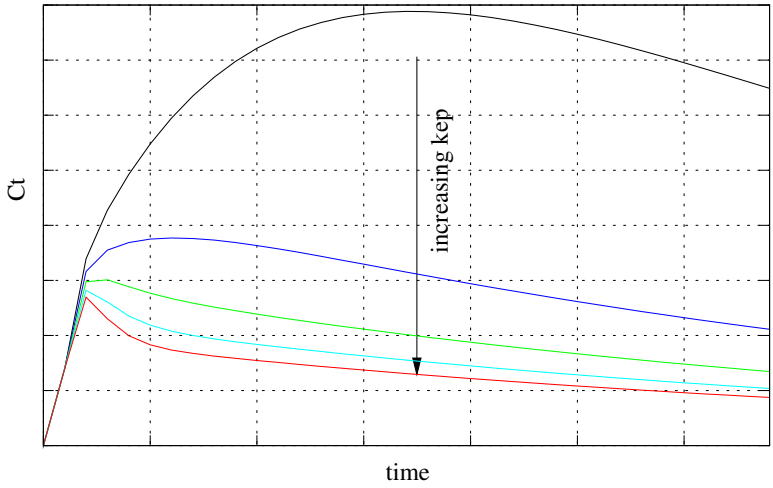

Figure 1.4: Simulated curves related to the gadolinium transport between the compartments. The influence of k_{ep} parameters is shown.

and disadvantages of each model, on its results we based the choice of a three parameters model, this model compared with the other two does not overestimate the parameters, and being less sensitive to local minima, does not require neither data interpolation nor supervised fitting.

So far, we saw that this model is used to fit the time curve concentration of contrast agent in the tissues. The curves are obtained by acquiring a dynamic sequence of T_1-weighted images, see section 2.2 on page 23, these images are then exploited to produce, for each pixel, a curve-concentration that feeds the model, after the fitting we have three images each one related to a physiological parameter, these images are referred to as *map*.

Chapter 2

Basics of MRI

In this chapter the basic principles of MRI are introduced with the intention of making more comprehensible next chapters.

2.1 Nuclear Spins and Magnetic Fields

In the present section, we will synthetically introduce the basic theoretical elements of a pulsed Nuclear Magnetic Resonance (NMR) experiment, adopting a semi-classical approach.

2.1.1 Spin and Magnetic Moment

Some atomic nuclei have an intrinsic property called spin. The existence of spin was first demonstrated in 1922 by the Stern Gerlach experiment, in which a beam of silver atoms were passed through a magnetic field and split into two beams. The two beams represent two states, up $|\uparrow\rangle$ and down $|\downarrow\rangle$ of the silver nuclei.The nuclear spin has an associated intrinsic angular momentum, a vector represented by the symbol **I**. According to the Heisenberg uncertainty principle, we can know simultaneously the length of **I**, together with only one of its components, conventionally assumed as the z-component, I_z:

$$|\mathbf{I}|^2 = \hbar[I(I+1)] \tag{2.1}$$

$$I_z = \hbar m \tag{2.2}$$

where $\hbar$ is Planck's constant divided by 2π, I is the spin quantum number and m is the magnetic quantum number, taking the following set of values: $m = (-I, -I+1, \ldots, I-1, I)$. In the case of spin 1/2 nuclei ($I = 1/2$), like ^{1}H, m can only be equal to $-1/2$ or $1/2$.

Nuclei having a spin angular momentum also have an associated magnetic moment, $\boldsymbol{\mu}$, given by:

$$\boldsymbol{\mu} = \gamma \mathbf{I} \tag{2.3}$$

$$\mu_z = \gamma I_z = \gamma \hbar m \tag{2.4}$$

where Eqn. 2.2 on the page before has been exploited and γ is the gyromagnetic ratio (sometimes called the magnetogyric ratio), a physical property of each nucleus. For a given abundance, nuclei with higher values of γ produce higher sensitivity NMR spectra. In fact, ^{1}H is the most commonly used isotope in magnetic resonance because of his abundance and sensitivity. All the experiments presented here employed ^{1}H, and all over the document we assume to deal with ^{1}H nuclei.

2.1.2 The effect of a Static Magnetic Field

During an NMR experiment, the sample is placed into a static magnetic field, generally referred to as $\mathbf{B_0}$. The energy of a magnetic moment immersed in $\mathbf{B_0}$ is given by:

$$E = -\boldsymbol{\mu} \cdot \mathbf{B_0} \tag{2.5}$$

The z reference axis is conventionally chosen along $\mathbf{B_0}$ and the magnitude of the field (coinciding with its z component) is referred to as B_0, i.e.

$$\mathbf{B_0} = B_0 \mathbf{k} \tag{2.6}$$

Substituting Eqn.s 2.6 and 2.4 in Eqn. 2.5, the energy of the nuclear spins of the sample can be written as:

$$E = -\mu_z B_0 = -\gamma I_z B_0 \tag{2.7}$$

or:

$$E_m = -m\gamma\hbar B_0 \tag{2.8}$$

where E_m is the energy of the spin state with the specific quantum number m.

In absence of field, the $|\uparrow\rangle$ and $|\downarrow\rangle$ states of a spin 1/2 system are equally populated, leading to zero net magnetization. When samples are placed into a magnetic field, a *small* excess of nuclei fall into the $|\uparrow\rangle$ state, according to the energy difference of the states, ΔE, and the Boltzmann distribution:

$$\Delta E = E_{|\downarrow\rangle} - E_{|\uparrow\rangle} = \gamma \hbar B_0 \tag{2.9}$$

$$\frac{N_{|\uparrow\rangle}}{N_{|\downarrow\rangle}} = \exp\left(\frac{\Delta E}{k_B T}\right) \tag{2.10}$$

where k_B is the Boltzmann's constant, T is the absolute temperature and $N_{|\uparrow\rangle}/N_{|\downarrow\rangle}$ is the ratio between the populations of the states. The nonzero energy difference between the spin states is known as the *Zeeman splitting* phenomenon.

The difference in population between the spin states, give rise to a non-null macroscopic magnetization vector, $\mathbf{M}$, defined as the vector sum of all the microscopic magnetic moments in the specimen:

$$\mathbf{M} = \sum_{i}^{N_s} \boldsymbol{\mu}_i \tag{2.11}$$

where $\boldsymbol{\mu}_i$ represents the magnetic moment of the ith nuclear spin and N_s is the total number of spins in the sample.

The fractional population difference at equilibrium in a typical clinical setup (protons in a magnetic field of 1.5 T at 300 K) is:

$$\frac{N_{|\uparrow\rangle} - N_{|\downarrow\rangle}}{N_{|\uparrow\rangle} + N_{|\downarrow\rangle}} = 5 \times 10^{-6} \tag{2.12}$$

This excess of spins accounts for the entire net magnetization *available* in the NMR experiment, thus explaining the relative low sensitivity of MRI, since only five part per million of protons can be measured. This should be compared with imaging techniques involving the decay of radioactive isotopes in which a single disintegration can be measured.

From Planck's law, $\Delta E = h\nu$, and Eqn. 2.9 on the preceding page, the frequency ν_0 of an NMR transition in a magnetic field B_0 is:

$$\nu_0 = \frac{\Delta E}{h} = \frac{\gamma B_0}{2\pi} \tag{2.13}$$

or, given $\nu_0 = \omega_0/2\pi$,

$$\omega_0 = \gamma B_0 \tag{2.14}$$

where ω_0 is known as the *Larmor precession frequency.*

2.1.3 Magnetization and Radio Frequency Pulses

A key role in a NMR experiment is played by circularly polarized (σ^-) radio frequencies pulses (rf), inducing the spin transitions by introducing rotating magnetic fields perpendicular to the main static field. The necessity of using (σ^-) polarized rf comes from quantum mechanical selection rules, dictating that NMR signals can only arise when the Δm of the corresponding transition equals -1. [13].

When placed in a variable magnetic field, the bulk magnetization (Eqn. 2.11) experiences a torque according to:

$$\frac{d\mathbf{J}(t)}{dt} = \mathbf{M}(t) \times \mathbf{B}(t) \tag{2.15}$$

where $\mathbf{J}(t)$ is the bulk spin angular momentum and $\mathbf{B}(t)$ is the sum of the static field $\mathbf{B_0}$ and, the rotating rf field $\mathbf{B_1}$:

$$\mathbf{B}(t) = \mathbf{B_0} + \mathbf{B_1}(t) \tag{2.16}$$

Substituting Eqn. 2.4 on page 18 in Eqn. 2.15 on the preceding page and multiplying each side by γ, we obtain:

$$\frac{d\mathbf{M}(t)}{dt} = \mathbf{M}(t) \times \gamma\mathbf{B}(t) \tag{2.17}$$

which is the basis of the Bloch equations.

In 1946 Felix Bloch formulated a set of equations that describe the behavior of a nuclear spin in a magnetic field, under the influence of rf pulses. He modified Eqn. 2.17 to account for the observation that nuclear spins relax to equilibrium values, following the application of rf pulses. Bloch assumed they relax, following first order kinetics, along the z-axis and in the x-y plane at different rates, designated $1/T_1$ and $1/T_2$, respectively. The relaxation processes regulated by the *characteristic times* T_1 and T_2 are called longitudinal (or *spin-lattice*) and transverse (or *spin-spin*) relaxation, respectively (see section 2.2 on page 23).

Adding the relaxation, Eqn. 2.17 becomes:

$$\frac{d\mathbf{M}(t)}{dt} = \mathbf{M}(t) \times \gamma\mathbf{B}(t) - \mathbf{R}(\mathbf{M}(t) - M_0) \tag{2.18}$$

where $\mathbf{R}$ is the relaxation matrix, defined as follows:

$$\mathbf{R} = \begin{pmatrix} 1/T_2 & 0 & 0 \\ 0 & 1/T_2 & \\ 0 & 0 & 1/T_1 \end{pmatrix} \tag{2.19}$$

and M_0 is the magnitude of the magnetization at thermal equilibrium. Eqn. 2.18 describes the motion of magnetization in the *laboratory frame*, an ordinary stationary coordinate system. Mathematically (and conceptually) the laboratory frame is not the simplest coordinate system, because the magnetization is moving at a frequency $\omega_0 = \gamma B_0$ in the x-y (transverse) plane. A simpler coordinate system is the *rotating frame*, in which the x-y plane rotates around the z-axis at a frequency $\Omega = -\omega_0$, below it is explained why the frequency of rotating frame equals the Larmor frequency.

Let us consider the magnetization (here for convenience of notation, the explicity time-dependence of magnetization and magnetic field is omitted):

$$\mathbf{M} = M_x\mathbf{i} + M_y\mathbf{j} + M_z\mathbf{k} \tag{2.20}$$

and its time derivative: [14]

$$\begin{aligned} \frac{d\mathbf{M}}{dt} &= \frac{\partial M_x}{\partial t}\mathbf{i} + \frac{\partial M_y}{\partial t}\mathbf{j} + \frac{\partial M_z}{\partial t}\mathbf{k} + M_x\frac{\partial \mathbf{i}}{\partial t} + M_y\frac{\partial \mathbf{j}}{\partial t} + M_z\frac{\partial \mathbf{k}}{\partial t} \\ &= \left(\frac{\partial M_x}{\partial t}\mathbf{i} + \frac{\partial M_y}{\partial t}\mathbf{j} + \frac{\partial M_z}{\partial t}\mathbf{k}\right) + M_x\frac{\partial \mathbf{i}}{\partial t} + M_y\frac{\partial \mathbf{j}}{\partial t} + M_z\frac{\partial \mathbf{k}}{\partial t} \end{aligned} \tag{2.21}$$

By knowing that:

$$\frac{\partial \mathbf{i}}{\partial t} = \boldsymbol{\omega} \times \mathbf{i} \tag{2.22}$$

and analogous ones for $\mathbf{j}$ and $\mathbf{k}$, Eqn. 2.21 on the preceding page becomes:

$$\begin{aligned} \left(\frac{d\mathbf{M}}{dt}\right)_{\text{lab}} &= \frac{\partial \mathbf{M}}{\partial t} + \boldsymbol{\omega} \times (M_x\mathbf{i} + M_y\mathbf{j} + M_z\mathbf{k}) \\ &= \left(\frac{\partial \mathbf{M}}{\partial t}\right)_{\text{rot}} + \boldsymbol{\omega} \times \mathbf{M} \end{aligned} \tag{2.23}$$

The total derivative represents the overall motion of $\mathbf{M}$ in the laboratory fixed frame, whereas the partial derivative represents the explicit dependence of $\mathbf{M}$ on time in the rotating frame (we can replace it with $\left(\frac{d\mathbf{M}}{dt}\right)_{\text{rot}}$). Substituting Eqn. 2.17 on the facing page in Eqn. 2.23, we obtain:

$$\begin{aligned} \left(\frac{d\mathbf{M}}{dt}\right)_{\text{rot}} &= \gamma\mathbf{M} \times \mathbf{B} - \boldsymbol{\omega} \times \mathbf{M} \\ &= \gamma\mathbf{M} \times (\mathbf{B} + \boldsymbol{\omega}/\gamma) \end{aligned} \tag{2.24}$$

The term $\boldsymbol{\omega}/\gamma$ has the dimension of a magnetic field and can be considerated a *fictitious* field that arises from the effect of the rotation. Alternatively we can rewrite Eqn. 2.24 in term of an *effective field*:

$$\left(\frac{d\mathbf{M}}{dt}\right)_{\text{rot}} = \gamma\mathbf{M} \times \mathbf{B}_{\text{eff}} \tag{2.25}$$

where:

$$\mathbf{B}_{\text{eff}} = \mathbf{B} + \boldsymbol{\omega}/\gamma \tag{2.26}$$

$$\mathbf{B}_{\text{eff}} = \mathbf{B}_0 + \boldsymbol{\omega}/\gamma + \mathbf{B}_1 = (B_0 - \omega_{\text{rf}}/\gamma)\mathbf{k} + B_1\mathbf{i} \tag{2.27}$$

The *resonance condition* is realized when the fictitious field exactly cancels $\mathbf{B}_0$ along z axis and leaves only $\mathbf{B}_1$ in the xy plane to interact with $\mathbf{M}$, or rather when its rotation frequency $\omega_{\text{rf}} = \Omega$ is equal ω_0 . The magnetization in the rotating frame acts as if the main $\mathbf{B}_0$ field had disappeared. The term

$$\omega_1 = \gamma B_1 \tag{2.28}$$

is the spin precession frequency generated by the circularly polarized rf field. This field makes the magnetization flip around the direction pointed by rf field in the rotating frame.

Eqn. 2.25 and 2.26 show that the ordinary equations of motion applicable in the laboratory system are valid in the rotating frame as well, provided that $\mathbf{B}_{\text{eff}}$ is used instead of $\mathbf{B}$. Thus in the rotating frame the magnetization precess about $\mathbf{B}_{\text{eff}}$ (which is static with respect to the rotating reference frame).

The transformation of Eqn. 2.18 on page 20 to the rotating frame is easily achieved by replacing each B_z (defined as B_0) by Ω/γ:

$$\begin{aligned}
\frac{dM_z(t)}{dt} &= \gamma[M_x(t)B_y^r(t) - M_y(t)B_x^r(t)] - \frac{M_z(t) - M_0}{T_1} \\
\frac{dM_x(t)}{dt} &= M_y(t)\Omega - M_z(t)\gamma B_y^r(t) - \frac{M_x(t)}{T_2} \\
\frac{dM_y(t)}{dt} &= M_z(t)\gamma B_x^r(t) - M_x(t)\Omega - \frac{M_y(t)}{T_2}
\end{aligned} \tag{2.29}$$

where the components of $\mathbf{B}$ are considered in the rotating frame.

Nuclear Magnetic Resonance earned its name in part because an rf pulse can only tip magnetization if its frequency is very close to the Larmor frequency. What happens when we apply a weak rotating field $\mathbf{B}_1$? If the rotation frequency of this field is very different from the Larmor frequency the effective field $\mathbf{B}_{\text{eff}}$ is directed practically along $\mathbf{B}_0$. The precession of $\mathbf{M}$ about $\mathbf{B}_{\text{eff}}$ has a very small amplitude and hardly modifies the direction of magnetic moment. On the other hand, if the resonance condition is satisfied, i.e. the rotation frequency of the field is exactly equal to the Larmor frequency, the precession of the magnetic moment then has a large amplitude and the magnetic moment can even be completely flipped.

2.1.4 Physical Interpretation of Bloch Equations

We will now examine the behavior of Eqn. 2.29 under two different limiting conditions, the effect of a short rf pulse and free precession. The rf pulse will be assumed to be very short compared to either relaxation times T_1 and T_2 as well as the inverse angular frequency Ω. This assumption is valid for many typical pulsed NMR experiments in which the pulse lengths can be as short as 5 μs. We will apply the rf pulse along the x-axis. These conditions allow us to neglect terms in Eqn. 2.29 that contain T_1, T_2, Ω and B_y:

$$\begin{aligned}
\frac{dM_z(t)}{dt} &= -M_y(t)\gamma B_x(t) \\
\frac{dM_x(t)}{dt} &= 0 \\
\frac{dM_y(t)}{dt} &= M_z(t)\gamma B_x(t)
\end{aligned} \tag{2.30}$$

Before solving Eqn. 2.30, it is worth a short digression to discuss the meaning of $B_x(t)$ and $B_y(t)$. Recall that B_0 is the static magnetic field strength oriented along the z-axis. $B_x(t)$ and $B_y(t)$ are magnetic fields oriented along the x-axis and y-axis that are generated by rf pulses. By analogy to $\omega_0 = \gamma B_0$ defining the frequency of the NMR transitions in the static magnetic field, we can see that the

terms $\gamma B_x(t)$ and $\gamma B_y(t)$ are frequencies of the magnetization $\mathbf{M}$ rotating around the x-axis or y- axis. Thus, applying these frequencies for different periods of time will allow for different degrees of rotation around the x-axis or y-axis. If we introduce a frequency of rotation about the x-axis as $\omega_x = \gamma B_x(t)$, solutions to Eqn. 2.30 on the preceding page are:

$$\begin{aligned} M_z(t) &= M_0 \cos \omega_x t \\ M_x(t) &= 0 \\ M_y(t) &= M_0 \sin \omega_x t. \end{aligned} \tag{2.31}$$

We define the *Flip Angle* (FA) as the pulse angle $\alpha = \omega_x t$ which makes the magnetization rotate about the direction pointed by rf, α is the angle between the direction of B_0 and the magnetization after the rf is turned off. Eqn. 2.31 shows that application of a magnetic field (rf pulse) along the x-axis causes the magnetization which was originally along the z-axis to rotate toward the y-axis by an angle α. Note that when $\alpha = 0$, $M_z(t) = M_0$ and $M_y(t) = 0$ (all the magnetization is still pointing along the z-axis). When $\alpha = 90°$, $M_y(t) = M_0$ and $M_z(t) = 0$ (all the magnetization is now pointing along the y-axis). Thus we have described the effects of a simple rf pulse.
The second limiting condition for Eqn. 2.29 on the preceding page is free precession in the absence of any applied pulse. In that case, B_x and B_y are both equal to zero, and Eqn. 2.29 on the facing page becomes:

$$\begin{aligned} \frac{dM_z(t)}{dt} &= -\frac{M_z(t) - M_0}{T_1} \\ \frac{dM_x(t)}{dt} &= M_y(t)\Omega - \frac{M_x(t)}{T_2} \\ \frac{dM_y(t)}{dt} &= -M_x(t)\Omega - \frac{M_y(t)}{T_2} \end{aligned} \tag{2.32}$$

One can verify that solutions to Eqn. 2.32 are:

$$\begin{aligned} M_z(t) &= M_z(0)e^{-\frac{t}{T_1}} + M_0(1 - e^{-\frac{t}{T_1}}) \\ M_x(t) &= (M_x(0)\cos \Omega t + M_y(0)\sin \Omega t)e^{-\frac{t}{T_2}} \\ M_y(t) &= (M_y(0)\cos \Omega t - M_x(0)\sin \Omega t)e^{-\frac{t}{T_2}} \end{aligned} \tag{2.33}$$

Eqn. 2.33 describes magnetization processing in the x-y plane at an angular frequency Ω while it is relaxing along the z-axis at a rate $1/T_1$ and relaxing in the x-y plane at a rate $1/T_2$.

2.2 Relaxation

It's worth spending some words about what happens to the magnetization after the rf irradiation is turned off. The magnetization returns to alignment with $\mathbf{B_0}$

by means of two kind of relaxation: the **spin-lattice** relaxation, characterized by the time T_1 and the **spin-spin** relaxation with a characteristic time denoted by T_2.

The return to equilibrium of the spin system via spin-lattice relaxation involves the transitions of protons from the higher energy level (*spin down*) to the lower energy level (*spin up*). Spin-lattice relaxation occurs because of the existence of magnetic fields fluctuating at the correct frequency in the $x - y$ plane which are able to induce transitions between the upper and lower energy levels of the protons in the static magnetic field. If these fluctuations are associated with the lattice then exchange of energy can occur between the spin system and the lattice. There are many physical processes that result in locally fluctuating magnetic fields. The most important of these in liquids is the **dipole-dipole** interaction. In water this relaxation is brought about by the random motion of water molecules (through rotation and diffusion) causing the magnetic fields generated by the dipole moments of the water molecules to fluctuate with time. These fluctuating fields will have components in the $x - y$ plane that oscillate at the Larmor frequency and will thus be able to induce transitions between upper and lower energy levels of nearby protons. The other important interactions that result in the transfer of energy from the spin system to the lattice are electric quadrupole, chemical shift anisotropy, indirect pseudo-dipolar, spin rotation and paramagnetic interactions. Typically T_1 ranges from $10^{-4} \div 10^4\ s$.

Quite different is the situation in case of **spin-spin** relaxation. Each proton produces a small magnetic field at its neighbor which falls off as r^{-3}. For water, each proton typically finds itself in a local field which ranges over $\pm 5 \times 10^{-4}\ T$. The static field B_0 is spread over this range and the resonance is no longer sharp. Thus individual protons will lose phase with each other simply because they precess at different frequencies. This results in ablation of the $x - y$ component in the rotating frame. A second de-phasing process also occurs for identical nuclei whereby nucleus j can induce transitions of nucleus k by producing oscillating magnetic moments at its Larmor frequency. Both these de-phasing processes produce broadening of the resonance absorption lines. The characteristic time for the phase memory of the spin system is denoted by T_2. However in practice other factors also contribute to de-phasing which do not depend on the nature of the substance being examined. The most important of these results from inhomogeneities in the static field B_0, which act like local field contributions to B_0 from other nuclei. It is found that

$$\frac{1}{T_2^*} = \frac{1}{T_2} + \frac{\gamma \Delta B_0}{2} \tag{2.34}$$

where T_2^* is the *observed or effective spin-spin relaxation time*, T_2 is the actual spin-spin relaxation time and ΔB_0 is the variation in the static magnetic field over the sample. ($T_2^* < T_2$).

2.3 Contrast agents

The aim of using a contrast agent in Magnetic Resonance Imaging (MRI) [15] is to help provide a clear picture by enhancing the *contrast* i.e. the relative difference of signal intensities in two adjacent regions of an image. Due to the T_1 and T_2 relaxation properties, differentiation between various tissues in the body is possible. This objective can be achieved by exploiting paramagnetic substances which can accelerating the relaxation of water protons in the surrounding tissue. Nowadays, Gd(III) complexes are by far the most widely used contrast agents in clinical practice. The choice of Gd(III) is explained by its seven unpaired electrons which makes it the most paramagnetic stable metal ion. Besides this, Gd(III) has another significant feature: owing to the symmetric S-state, its electronic relaxation is relatively slow which is relevant to its efficiency as an MRI contrast agent. A Gd(III) complex induces an increase of both the longitudinal and transverse relaxation rates, $1/T_1$ and $1/T_2$, respectively, of the solvent nuclei. The observed solvent relaxation rate, $1/T_{i,obs}$, is the sum of the diamagnetic $(1/T_{i,d})$ and paramagnetic relaxation rates $(1/T_{i,p})$:

$$\frac{1}{T_{i,obs}} = \frac{1}{T_{i,p}} + \frac{1}{T_{i,d}}, \text{ where } i = 1, 2 \tag{2.35}$$

The diamagnetic term, $(1/T_{i,d})$, corresponds to the relaxation rate of the solvent (water) nuclei in absence of a paramagnetic solute. The paramagnetic term, $(1/T_{i,p})$, gives the relaxation rate enhancement caused by the paramagnetic substance, which is linearly proportional to the concentration of the paramagnetic species, [Gd]:

$$\frac{1}{T_{i,obs}} = \frac{1}{T_{i,d}} + r_i[Gd], \text{ where } i = 1, 2 \tag{2.36}$$

According to Eqn. 2.36, a plot of observed relaxation rates versus the concentration of the paramagnetic species gives a straight line and its slope defines the relaxivity, r_i (in units of $\mathrm{mM^{-1}s^{-1}}$). If we consider the relaxation of water protons, which is the basis of imaging by magnetic resonance, we can introduce the corresponding term *proton relaxivity*. The simple term *relaxivity* is very often used in the context of MRI contrast agents and always refers to *longitudinal proton relaxivity*, even if the adjectives are omitted.

The paramagnetic relaxation of the water protons originates from the dipole-dipole interactions between the nuclear spins and the fluctuating local magnetic field caused by the unpaired electron spins. This magnetic field around the paramagnetic center vanishes rapidly with distance. Therefore, specific chemical interactions that bring the water protons into the immediate proximity of the metal ion play an important role in transmitting the paramagnetic effect towards the bulk solvent. For Gd(III) complexes, this specific interaction corresponds to the binding of the water molecule(s) in the first coordination sphere of the metal

ion. These inner-sphere water protons then exchange with bulk solvent protons and this way the paramagnetic influence is propagated to the bulk. This mechanism is depicted as the inner-sphere contribution to the overall proton relaxivity. Solvent molecules of the bulk also experience the paramagnetic effect when they diffuse in the surroundings of the paramagnetic center. The effect of the random translational diffusion is defined as outer-sphere relaxation. Thus we separate the inner and outer-sphere contributions based on the intra and intermolecular nature of the interaction, respectively. The total paramagnetic relaxation rate enhancement due to paramagnetic agent is therefore given as

$$\left(\frac{1}{T_{i,p}}\right) = \left(\frac{1}{T_{i,p}}\right)^{IS} + \left(\frac{1}{T_{i,p}}\right)^{OS} \tag{2.37}$$

or

$$r_i = r_i^{IS} + r_i^{OS} \tag{2.38}$$

where the superscripts 'IS' and 'OS' refer to the inner and outer sphere, respectively.

2.4 Signal from Precessing Magnetization

The fundamental signal in a MR experiment comes from the detection of the *emf* predicted by following equation for precessing magnetization: [16]

$$emf \equiv E = -\frac{d}{dt}\Phi_M(t) = -\frac{d}{dt}\int_{\text{sample}} d^3r \mathbf{M}(\mathbf{r},t)\cdot\mathbf{B}_1(\mathbf{r}) \tag{2.39}$$

where $\Phi_M(t)$ is the time-varying magnetic flux through the coil (a loop of wire), $\mathbf{B}_1(\mathbf{r})$ is the receive field produced by the detection coil at all points where the magnetization is nonzero.
It's assumed that the sample is immersed in a static, uniform field B_0 and has been excited by some rf pulse so that there exist, at time t, transverse components, M_x, M_y of magnetization, in addition to a longitudinal component, M_z. A common configuration is to use the same rf coil to transmit $\mathbf{B}_1$ fields to the object and to receive signal from the magnetization. Assume, for a given coil configuration and current I_1, the rf field generated is $\mathbf{B}_1$. By the principle of reciprocity, the coils receive sensitivity can be defined as:

$$\mathbf{C}_1 = \mathbf{B}_1/I_1 \tag{2.40}$$

The incremental voltage produced by magnetization in an element $d\mathbf{r}$ is:

$$dE = -\mathbf{C}_1(\mathbf{r})\cdot\frac{\partial}{\partial t}\mathbf{M}(t)d\mathbf{r} \tag{2.41}$$

Now suppose our magnetization comes from a precessing spins having magnetization M_{xy} in the presence of a magnetic field of size B_0. That is:

$$\mathbf{M}(t) = \begin{pmatrix} M_{xy}\cos(\omega_0 t) \\ -M_{xy}\sin(\omega_0 t) \\ 0 \end{pmatrix} \tag{2.42}$$

and suppose the coil is positioned in $x-y$ plane making the sensitivity lines (flux lines) point in the y-direction:

$$\mathbf{C}_1 = \begin{pmatrix} 0 \\ C \\ 0 \end{pmatrix} \tag{2.43}$$

The voltage induced in the coil, which will become our received signal $S_{\text{rec}}(t)$, can then be shown to be:

$$S_{\text{rec}}(t) = dE = M_{xy}\omega_0 C\cos(\omega_0 t) \tag{2.44}$$

If we include T_2 relaxation, the signal received will look like that in figure 2.1 on the following page. The signal is known as Free Induction Decay (FID). FID [17] arise from the action of a single pulse on a nuclear spin system. *Free* refers to the fact that the signal is generate by the free precession of the bulk magnetization vector about the B_0 field; *induction* indicates that the signal was produced based on Faraday's law of electromagnetic induction; and *decay* reflects the characteristic decrease with time of signal from a spin system after a pulse excitation. FID signals are the most basic form of transient signals from a spin system after a pulse excitation. They are also the mother signal for other forms of MR signals. Mathematically, an FID signal resulting from an α pulse takes the following form:

$$S(t) = \sin(\alpha)\int_{-\infty}^{\infty}\rho(\omega)e^{-t/T_2(\omega)}e^{-i\omega t}d\omega \quad t \geqslant 0 \tag{2.45}$$

Clearly, the spectral density function $\rho(\omega)$ determines the characteristic of an FID signal. For example, the FID signal of a spin system with a single spectral component resonating at the frequency ω_0 can be expressed as:

$$S(t) = M_z^0 \sin\alpha\ e^{-t/T_2} \quad t \geqslant 0 \tag{2.46}$$

Two basic parameters of an FID signal are its amplitude and decay rate, see figure 2.1 on the next page.

2.5 From Spectra to Images

In this section we will face the principles at the bases of MRI and the main imaging pulse sequences will also be introduced.

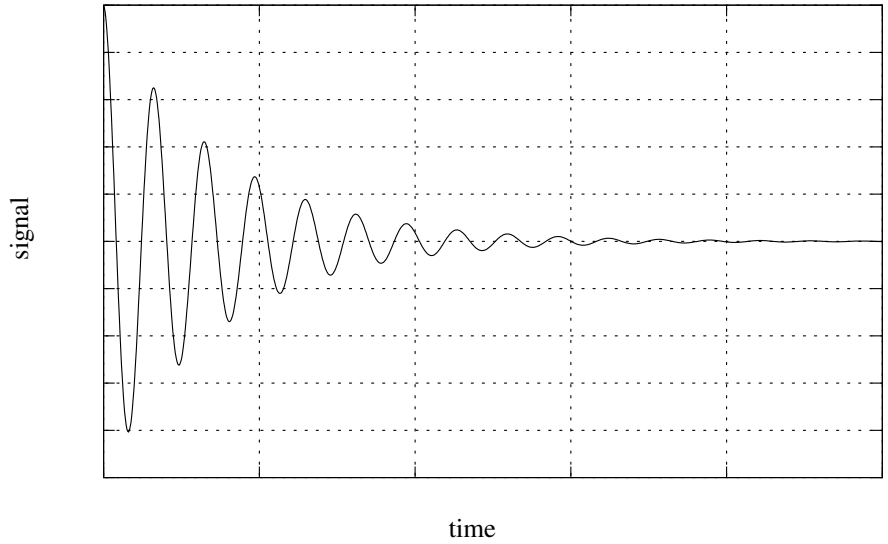

Figure 2.1: A typical FID.

2.5.1 The Effect of Magnetic Field Gradients

In conventional NMR spectroscopy the spectrum of nuclear precession frequencies gives information about the chemical environment of the spins and it is important to arrange that the esternal static field, B_0, should vary as little as possible across the sample. By contrast, the key element of an imaging experiment is the presence of gradients varying linearly the field magnitude across the sample, in order to encode the signal of the spins in the space.

In two-dimensional (2D) *Fourier Imaging*, one of the most common imaging technique, the spatially localized magnetic resonance information is obtained through the sequential application of three perpendicular pulsed gradients. Each gradient has a different effect, generally referred to as *slice selection*, *phase encoding* and *frequency encoding*, see below.

Slice Selection

Slice selection (or selective excitation) is performed by applying a magnetic field gradient during the rf excitation. Often, the direction of the slice selective gradient is chosen along z (the direction of the static magnetic field, $\mathbf{B_0}$) so, for sake of simplicity, here we will consider only this case, referring to the *slice selection gradient* as G_z, where:

$$G_z = \frac{\partial B}{\partial z} \tag{2.47}$$

Analogous definitions take G_x and G_y, introduced below. It is worth stressing that, in any case, only the magnitude of the static field is influenced by the gradients, whereas the direction of $\mathbf{B_0}$ remains constant all over the sample. In

presence of G_z the Larmor frequency becomes a function of z, i.e.

$$\omega = -\gamma(B_0 + G_z z) \tag{2.48}$$

By exciting the sample with an rf, whose angular frequency (ω_{rf}) is given by Eqn. 2.48, only the spins about $z = -(\omega_{\text{rf}} + \gamma B_0)/(\gamma G_z)$ will be nutated into the x-y plane, contributing to the final signal, thus selecting a plane of the sample perpendicular to $\mathbf{B}_0$.

For a rectangular rf pulse of duration T, there will be a spread of frequencies described by the *Fourier Transform* (FT) of a rectangular window function, i.e. a sinc function centered on ω_{rf}, with a bandwidth proportional to $1/T$. The approximate width of the slice selected will thus be:

$$\Delta z = \frac{1}{\gamma G_z T} \tag{2.49}$$

hence duration of the rf pulse is the principal means to control slice thickness. A slice profile that is a sinc function however is not ideal, as it produces substantial excitation in the wings away from the selected slice. Improved slice profiles can be obtained by using excitation pulses of different shapes, like sinc or Gaussian.

Phase and Frequency Encoding

Once the slice has been excited, the frequency and phase of the precessing macroscopic magnetic moment can be made a function of position within the slice. In the simplest case, if a magnetic field gradient in the x-direction, G_x, is switched on during the signal acquisition, then the Larmor frequency becomes a function of x (*frequency encoding*):

$$\omega(x) = -\gamma(B_0 + G_x x) \tag{2.50}$$

and the slice is cut into *strips* of constant Larmor frequency. Ignoring the T_2 decay, an area $dxdy$ in the selected slice gives a contribute $dS(t)$ to the total FID signal:

$$dS(t) = \rho(x, y) e^{-i\gamma(B_0 + G_x x)t} dxdy \tag{2.51}$$

where ρ is the proton density function. Demodulating the signal, to remove the carrier frequency γB_0, and identifying:

$$k_x = \gamma G_x t \tag{2.52}$$

the total FID is given by:

$$S(k_x) = \int \underbrace{\int \rho(x, y) dy}_{\rho \text{ projection}} e^{-ik_x x} dx \tag{2.53}$$

which is the FT of a ρ projection along y. Note that k_x is a function of the time.

The ρ projection along y can be resolved applying, for a certain amount of time, a gradient along y, immediately following selective excitation and just before signal acquisition. By briefly turning on the G_y field gradient, the precessional phases of the rotating macroscopic magnetization can be manipulated as follows. G_y induces a variation of the Larmor frequency along the y-direction, according to:

$$\omega(y) = -\gamma(B_0 + G_y y) \tag{2.54}$$

If G_y is now turned off after a time τ_y, $\mathbf{M}$ returns to the constant frequency ω_0, but having accumulated a phase shift, ϕ, as a function of y (*phase encoding*), i.e.

$$\phi(y) = \gamma G_y y \tau_y \tag{2.55}$$

If the frequency encoding gradient is now turned on and the signal acquired, then the FID is a function of t and τ_y i.e.

$$\begin{aligned} S(t, \tau_y) &= \int\int \rho(x, y) e^{-i(\gamma G_x x t + \phi(y))} dx dy \\ &= \int\int \rho(x, y) e^{-i(\gamma G_x x t + G_y y \tau_y)} dx dy \end{aligned} \tag{2.56}$$

Using G_x and G_y we have indexed each nutated macroscopic magnetic moment in the selected slice, that is, each (x, y) position, with an unique combination of *Larmor frequency* and *Larmor phase*, (ω, ϕ).

2.5.2 k-Space and Pulse Sequences

In analogy with Eqn. 2.52 on the page before, we can define k_y as:

$$k_y = \gamma G_y \tau_y \tag{2.57}$$

and rewrite Eqn. 2.56 as:

$$S(k_x, k_y) = \int\int \rho(x, y) e^{-i(k_x x + k_y y)} dx dy \tag{2.58}$$

The plane defined by the $\mathbf{k} = (k_x, k_y)$ points plays an important role in the interpretation of MRI experiments, and it is called *k-space*.

Recognizing in Eqn. 2.58 that $S(k_x, k_y)$ and $\rho(x, y)$ are *FT pairs*, the proton density over the slice (i.e. the *image*) can be obtained by taking the inverse 2D FT of the demodulated FID over the k-space. k_y is varied by stepping through different values of G_y, whereas k_x is sampled by holding on the frequency encoding gradient and sampling the FID.

From the properties of the FT, we know that the signal acquired at each k-space location contains information about the whole image, but the *type* of

information varies across the k-space. Most of the contrast of the final image is encoded at the center of the k-space (small k_x and k_y), while its periferic part accounts mainly for the high frequency contributes to the image, that is, resolution of details and noise.

Repetition Time and T_1-Weighted Images

The acquisition of each *line* of the k-space (i.e. $\forall\ (k_x,\ k_y)\ k_y = \text{const}$) implies an rf pulse, a series of gradient pulses, and the signal acquisition. Then, according to the T_1 value of the sample, a certain amount of time has to be waited to let the longitudinal magnetization to recover, before the acquisition of the next line. The time course between two subsequent excitation rf pulses is called *repetition time*, and referred to as T_R, while the sequence of gradient and rf pulses is known as *pulse sequence*. The total acquisition time of a slice, T_{acq} is then given by:

$$T_{\text{acq}} = N_y T_R \tag{2.59}$$

where N_y is the number of k_y steps.

Usually, T_R is often set to do not let the magnetization completely recover the thermodynamic equilibrium before the subsequent rf pulse ($T_R \leq T_1$). After a few pulses, the recovered value of M_z reaches a *steady state*, depending upon the T_1 of the sample, but always lower than M_0.

The longitudinal magnetization after the nth T_R interval is given by:

$$\begin{aligned} M_z^{(n)} &= M_z^{(n-1)} \cos\theta + (1 - e^{-T_R/T_1})(M_0 - M_z^{(n-1)} \cos\theta) \\ &= (1 - e^{-T_R/T_1})M_0 + K M_z^{(n-1)} \end{aligned} \tag{2.60}$$

where θ is the FA of the excitation pulse (see section 2.1.4 on page 22) and:

$$K = \cos\theta e^{-T_R/T_1} \tag{2.61}$$

Writing Eqn. 3.10 as a sequence we have:

$$\begin{aligned} M_z^{(n)} &= (1 - e^{-T_R/T_1})M_0(1 + K + K^2 + \ldots + K^n) + K^n e^{-T_R/T_1} M_0 \\ &= (1 - e^{-T_R/T_1})M_0 \frac{1 - K^{n+1}}{1 - K} + K^n e^{-T_R/T_1} M_0 \end{aligned} \tag{2.62}$$

and, since $K < 1$, for $n \to \infty$, the steady state value is:

$$M_z^{(n\to\infty)} = M_z^{\text{steady}} = \frac{(1 - e^{-T_R/T_1})M_0}{(1 - K)} \tag{2.63}$$

A short T_R, together with reducing T_{acq}, can thus be used to induce a contrast between two parts of the sample having the same ρ, but different T_1 (T_1-*weighted image*).

Multi-Slice 2D Imaging

The coverage of a 3D volume is accomplished through the *multi-slice* approach, by applying a sequence of rf pulses, exciting different slices, within a single T_R. During each T_R, one k-space line is acquired for all the slices, thus keeping the same T_{acq} of the single-slice acquisition. On the other hand, T_R has to be set long enough to allow for the pulse sequence of each slice being executed.

Because of imperfect rf profiles, the immediate neighborhood of an excited slice is also partly excited (*slice cross-talk effect*). In multi-slice imaging, this region cannot be included in the following slice since the spins do not have time to recover toward equilibrium. To overcome the problem, it is common either to leave a gap between slices, or to excite the odd numbered slices first and the even numbered ones afterwards.

2.5.3 3D Volume Imaging

As an alternative to the 2D multi-slice approach for imaging 3D volumes, the 2D coverage of k-space described in section 2.5.1 on page 28 can be generalized to 3D.

The excitation pulse is used to select a thick *slab* of the sample, then the 3D k-space is discretely sampled in both directions, k_y and k_z, through phase encoding. The read sampling along the x-direction is carried out, as in 2D, with measurements at finite time steps Δt during the continuous application of a gradient G_x. The associated step in the k_x direction is:

$$\Delta k_x = \gamma G_x \Delta t \tag{2.64}$$

The (k_y,k_z) position of each acquisition line is determined by applying the orthogonal gradients G_y and G_z, for the τ_y and τ_z time intervals, respectively. The corresponding steps in k-space are:

$$\Delta k_y = \gamma \Delta G_y \tau_y \tag{2.65}$$

$$\Delta k_z = \gamma \Delta G_z \tau_z \tag{2.66}$$

where ΔG_y is the difference in G_y intensity between two consecutive read lines, and analogously for ΔG_z.

Under 3D imaging conditions, the signal from a single rf excitation of the whole sample can be written as a 3D FT of the proton density:

$$\begin{aligned} S(k_x, k_y, k_z) &= \int\int\int dx dy dz \rho(x, y, z) e^{-i2\pi(k_x x + k_y y + k_z z)} \\ &= F[(\rho(x, y, z)] \end{aligned} \tag{2.67}$$

3D vs 2D Imaging

3D imaging presents several advantages in comparison with multi-slice imaging:

1. The ability to change the number of the N_z phase encoding steps over the excited slab, of thickness TH, gives the control over the size of the partition thickness $\Delta z = TH/N_z$ without any limitation on the rf amplitude or duration. In general, higher z resolutions are obtainable.

2. The signal-to-noise ratio can be enhanced, thanks to the higher flexibility in setting the pulse program parameters available in 3D imaging, but achieving this may come at the expense of increased imaging time. [18]

3. Consecutive slices may be adjacent without cross-talk effects.

4. Shorter T_R are usable if necessary, since only one k-space line has to be acquired each repetition.

On the other hand, the total acquisition time for 3D imaging is given by:

$$T_{\text{acq}} = N_y N_z T_R \tag{2.68}$$

where N_y and N_z denote the number of phase encoding steps along y and z. As evident from the Eqn.s 2.59 on page 31 and 2.68 the 2D imaging lasts much shorter time with respect to the 3D imaging.

An immediate consequence is the capability of acquiring more 2D than 3D images within the same time, thus allowing a higher temporal resolution, in dynamic studies, or the averaging of data, for increasing the signal-to-noise ratio. A more indirect effect is due to the capability (but also the necessity, see section 2.5.2) of setting longer T_R, given a certain T_{acq}, in multi-slice imaging. A longer T_R implies a higher steady-state value of the longitudinal magnetization, thus giving a higher signal.

2.5.4 SNR dependence on imaging parameters

The SNR (signal to noise ratio) dependence on imaging parameters is complicated by the noise behavior. Noise depends on many different imaging parameters such as the number of acquisition N_{acq}, the number of k-space samples N_x, N_y, N_z the redout bandwidth dependence and voxel dimensions Δx, Δy, Δz (or TH in 2D). SNR is given by: [16]

$$SNR/voxel \propto \frac{\Delta_x \Delta_y \Delta_z \sqrt{N_{acq}}}{\sqrt{\frac{BW_{read}}{N_x N_y N_z}}} \tag{2.69}$$

Substituting $\Delta t = 1/BW_{read}$ gives:

$$SNR/voxel \propto \Delta_x \Delta_y \Delta_z \sqrt{N_{acq} N_x N_y N_z \Delta t} \tag{2.70}$$

Since $T_s = N_x \Delta t$, substituting this into Eqn. 2.70 on the preceding page yields:

$$SNR/voxel \propto \Delta_x \Delta_y \Delta_z \sqrt{N_{acq} N_y N_z T_s} \tag{2.71}$$

The expression in Eqn. 2.71 can be rewritten for a 2D imaging experiment. The voxel has now dimension of $\Delta_x \times \Delta_y \times TH$. Also, N_z is replaced by unity. Therefore,

$$(SNR/voxel)\,|_{2D} \propto \Delta_x \Delta_y TH \sqrt{N_{acq} N_y T_s} \tag{2.72}$$

In other words, a 2D imaging experiment performed with exactly the same image parameters (including T_R,T_E and FA) with $\Delta_z = TH$ has $\sqrt{N_z}$ worse SNR in comparison with the 3D imaging experiment. However, the 2D imaging experiment requires an imaging time which is N_z times shorter than 3D experiment, we can take advantage from this and perform more than one acquisition of the same slab, by averaging over these slabs it is possible to increase the SNR even in 2D imaging experiment.

2.5.5 Gradient Recalled Echo Sequence

In the imaging sequences described so far, we always assumed to acquire FID signals (see section 2.4 on page 26), however this is almost never done in practice. In fact, after excitation and phase encoding, the *echo* of the original FID is recalled by means of the read gradient, and measured (*gradient recalled echo*, GRE). The reason for this is best explained by inspecting the meaning of FID and echo acquisitions in the k-space formalism.

Let us watch at the FID as first, and let us consider Eqn. 2.52 on page 29. Up to the acquisition start, G_x is turned off, so $k_x = 0$, while k_y is determined by the phase-encoding (Eqn. 2.57 on page 30). In other words, at the acquisition beginning the $\mathbf{k}$ point is located somewhere on the k_y axis. When G_x is turned on, k_x increases linearly in time, that is, $\mathbf{k}$ travels along a line parallel to the k_x axis in the positive direction, stepping according to the sampling frequency (Eqn. 2.64 on page 32). The $\mathbf{k}$ trajectory is shown with blue arrows in Fig. 2.2(a), note that only the $k_x > 0$ half of the k-space is sampled.

In the echo scheme, a negative read gradient ($G_x = -G_-$ where $G_- > 0$) is applied in the time interval τ_-, before starting the acquisition. As a consequence, $\mathbf{k}$ moves in the negative k_x direction up to $k_x = -\gamma G_- \tau_-$, and spins along x dephase according to:

$$\phi_G(x) = -\gamma G_x x \tau_- = +\gamma G_- x \tau_- \tag{2.73}$$

canceling the signal.

G_x is then switched to the positive value G_+ and the acquisition started. $\mathbf{k}$ reverts its motu, traveling in the positive k_x direction, and the spins start refacing,

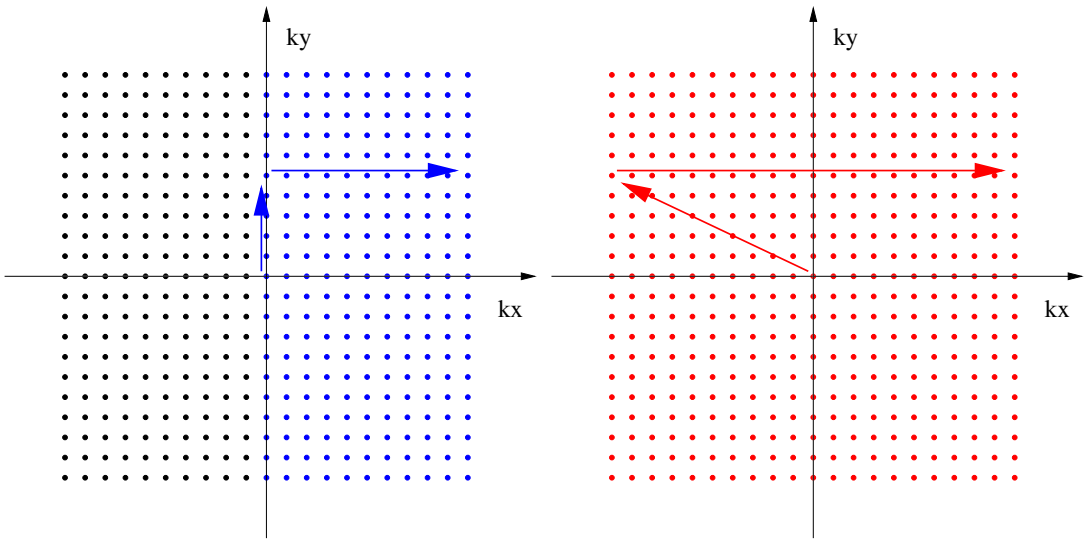

(a) FID sampling (b) Echo sampling

Figure 2.2: **k** trajectories across the k-space for the FID and echo sampling schemes. The visited sampling points in the two cases are shown as colored points.

increasing the signal. The phase coherence is completely recovered (the center of the echo) after the time τ_+, when:

$$\phi_G^{\text{echo}}(x) = \underbrace{+\gamma G_- x \tau_-}_{G_x<0} \underbrace{-\gamma G_+ x \tau_+}_{G_x>0} = 0 \tag{2.74}$$

and **k** reaches the k_y axis. The last part of the echo scheme resample the FID acquisition: the G_x gradient is held on for another τ_+, **k** moves in the $k_x > 0$ half and the signal cancels away again.

The time interval between the rf excitation and the center of the echo is called *echo time* and it is referred to as T_E. In order to minimize T_E (see below), the negative lobe of G_x is usually applied contemporaneously to G_y, and the general condition for having a GRE is:

$$\int_{T_E} G_x(t)dt = 0 \tag{2.75}$$

The **k** trajectory for the full echo sampling is shown with red arrows in Fig. 2.2(b), while the scheme of the sequence, with the basic elements discussed above, is represented in Fig. 2.3. Standard conventions for the sequences schematization have be adopted. [19]

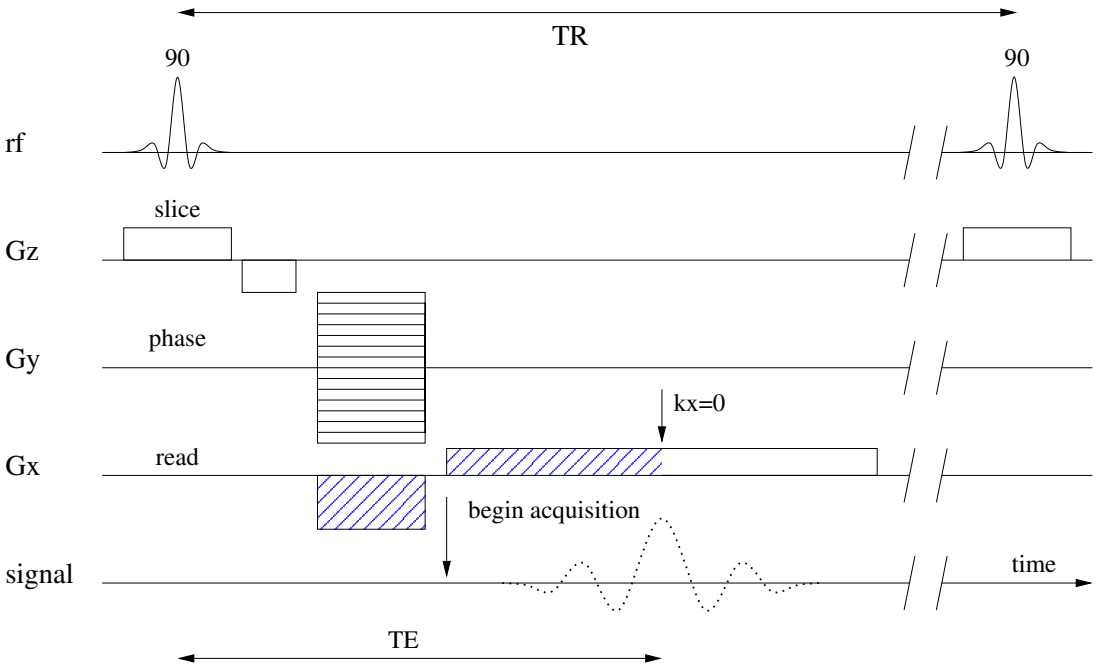

Figure 2.3: Scheme of the basic elements of the GRE sequence. The dashed blue areas of the read gradient represent the echo condition expressed Eqn.2.74. T_R and T_E are also reported.

Why Using Echoes and T_2-Weighted Images

The full echo sampling scheme confers two advantages over the FID acquisition:

- The double of the sampling k-points are acquired, so there is a factor 2 of signal-to-noise gain.
- The signal is sampled in a raster of $\mathbf{k}$ points centered at the k-space origin, therefore there is not dispersion spectrum and $\rho(\mathbf{r})$ can be calculated directly by taking the modulus of the resulting FT.

There is, however, a difficulty with the full echo sampling scheme where T_2 relaxation is significant. The acquisition of the maximum of the signal is delayed at the center of the echo, when part of the transverse magnetization is already lost. The effect is even enhanced by the inhomogeneities in the static field introduced by the gradients, reducing the transverse relaxation time according to:

$$\frac{1}{T_2^*} = \frac{1}{T_2} + \frac{\gamma \Delta B_0}{2} \tag{2.76}$$

where T_2 is the spin-spin relaxation time with homogeneous filed, ΔB_0 is the variation in the static magnetic field over the sample and T_2^* is the *observed* or *effective* spin-spin relaxation time ($T_2^* < T_2$).

In order to maximize the signal, the minimum echo time should be chosen. A longer T_E can, however, be employed to get an image contrast between areas having different T_2, thus obtaining a T_2-*weighted image*.

Spoiling Residual Magnetization

If T_R is set very short ($T_R \simeq T_2^*$), a fraction of the transverse magnetization of the preceding repetition can still be present at the acquisition time, disturbing the signal. The *spoiling* is the method by which residual transverse magnetization is destroyed deliberately prior to the excitation pulse of the subsequent repetition. Sequences may be rf spoiled or gradient spoiled, or both.

rf spoiling involves applying a phase offset to each successive rf excitation pulse. Think of it as the same flip angle but in a different direction, so that the residual magnetization in the x-y plane always points in a different direction, preventing any build up towards a steady state.

Gradient spoiling occurs after each echo by using strong gradients after the frequency encoding. Spins in different locations, experiencing a variety of magnetic field strengths, precess at differing frequencies, thus, dephasing.

GRE Signal

The image signal for a GRE sequence is given by:

$$I = A\frac{(1 - e^{-T_R/T_1})\sin\theta}{1 - e^{-T_R/T_1}e^{-T_R/T_2^*} - \cos\theta(e^{-T_R/T_1} - e^{-T_R/T_2^*})} \tag{2.77}$$

where A is a constant which takes into account the proton density and the receiver gain as well, θ is the FA of the excitation pulse, whereas T_1, T_2^* and T_R have their usual meaning.

When $T_R \gg T_2^*$ then e^{-T_R/T_2^*} approaches zero and under conditions of perfect spoiling of transverse magnetization Eqn. 2.77 reduces to:

$$I = A\frac{(1 - e^{-T_R/T_1})\sin\theta}{1 - \cos\theta e^{-T_R/T_1}} \tag{2.78}$$

Recalling now Eqn. 3.12 on page 54, from their similarity, we can deduce that Eqn. 2.78 describe the steady state signal and that can be analogously derived.

However, since an echo, not the FID, is acquired in GRE sequence, the signal is reduced by a factor of e^{-T_E/T_2^*} accounting for the T_2^* decay occurred during T_E; Eqn. 2.78 becomes:

$$I = A\frac{(1 - e^{-T_R/T_1})\sin\theta}{1 - \cos\theta e^{-T_R/T_1}}e^{-T_E/T_2^*} \tag{2.79}$$

The dependence upon T_R and FA of the GRE signal, as expressed in Eqn. 2.78, is shown in Fig. 2.4 on the next page. Note how the FA corresponding to the maximum signal, conventionally called *Ernst angle*, increases with T_R.

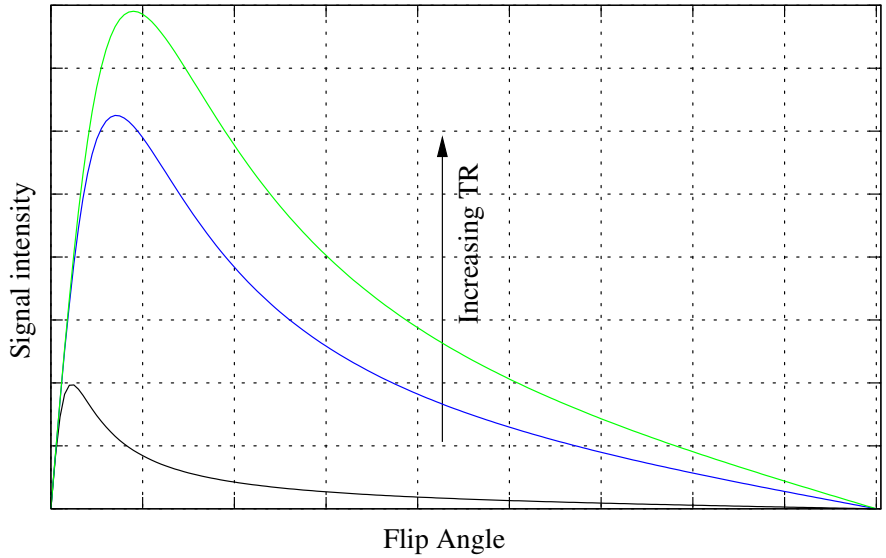

Figure 2.4: Symulated GRE signal intensity, as expressed in Eqn. 2.78, vs FA. A and T_1 are set to 1 and 1000 ms, respectively, while $T_R = 5$, 50, 80 ms.

2.5.6 Spin Echo Sequence

In spectroscopic NMR sequences, signal echoes are obtained through a 180° rf pulse following the excitation pulse.

Immediately after a 90°_x excitation pulse, in the rotating reference frame, the magnetization lies on the y-axis. Due to field inhomogeneities, spins start dephasing by precessing in opposite directions and at different speed. If, after a time τ, a 180°_y pulse is applied, the spins are *flipped* around y so that, conserving their angular velocity, they start rephasing. After another τ, the spins are back in phase to give a *spin echo* (SE), where $T_E = 2\tau$.

In SE imaging sequences rf and gradient pulses are arranged so to synchronize the gradient and spin echoes. Thanks to the y-axis flipping caused by the 180 rf pulse, the dephasing due to field gradients is recovered completely. In other words, the only source of signal reduction is the *pure* spin-spin T_2 relaxation, resulting in a net signal gain over GRE (where T_2^* is acting, see the previous section).

The main limit of SE imaging is that T_R can not be set as short as in GRE, due to the higher complexity of the sequence. However, by making T_R long compared to T_E, it is possible to generate several spin echoes in one T_R interval. This is successfully utilized in *fast spin echo* (FSE) sequences, where single 90° pulse is followed by several 180° pulses. Each 180° pulse creates an echo, which is individually phase encoded, and several k-space lines of the same slice can thus be acquired following a single excitation.

Within T_R, the transverse magnetization is subject to T_2 relaxation, so last echoes of each repetition are strongly T_2-weighted, and the resulting image is

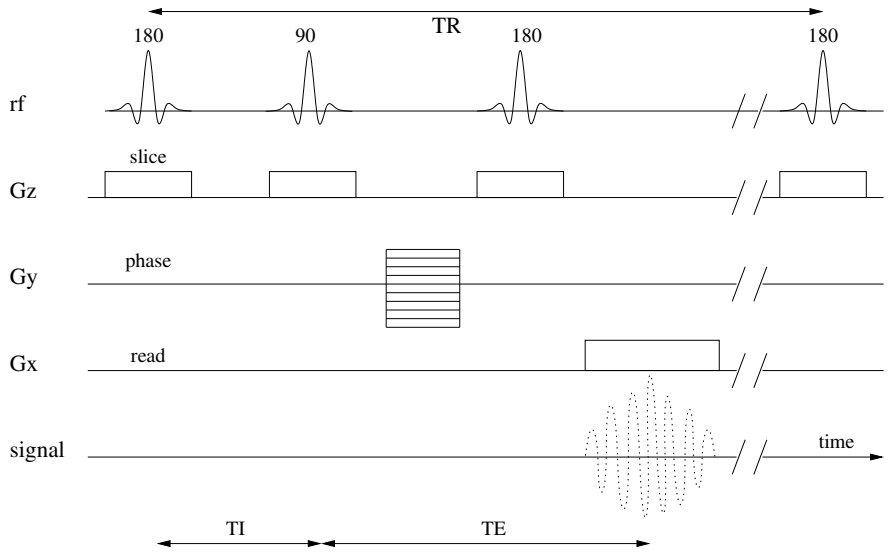

Figure 2.5: Basic part of an inversion recovery sequence.

T_2-weighted as well.

2.5.7 The inversion recovery sequence

Inversion recovery, [19] is used for measurement of T_1 relaxation times as well as for the selective suppression of unwanted spin signals. The first 180° rf pulse inverts the magnetization vector, so subjecting the system to the most severe disturbance from equilibrium. Spin-lattice relaxation proceeds for a time t following which a 90° pulse is used to inspect the remaining longitudinal magnetization. The time $t = T_I$, *Inversion Time*, has been defined as the time of 90° pulse, see figure 2.5. In imaging, the signal is usually refocused with a 180 degree pulse as in a spin echo sequence. The signal amplitude is described by

$$M(t) = M_0(1 - 2e^{-t/T_1}). \tag{2.80}$$

After the longitudinal magnetization is tipped into the transverse plane to provide the initial signal, the magnitude of the transverse magnetization evolves as

$$M_\perp = |M_0(1 - 2e^{-T_I/T_1})|e^{-(t-T_1)/T_2^*} \quad t > T_I \tag{2.81}$$

A noteworthy feature of this method is the change from negative signal (proportional to $-M_0$) at $t = 0$ to a positive signal (proportional to M_0) as t becomes large. The cross-over through zero magnetization occurs at $t = 0.6931T_1$ and can be exploited to several effect. First, it is clear that a measurement of time for the cross-over null can yield T_1 in a single measurement. Second, the method may be used to remove the contribution from a spin with specific T_1 value by applying a 180° pulse at a time interval $t = 0.6931T_1$ before the imaging pulse sequence.

Chapter 3

Imaging protocol for T_1 measurements

As introduced in chapter 1 on page 7, quantitative analysis of tumor perfusion requires the knowledge of the tracer time concentration curves. These curves can then be fitted by means of the model described in the section 1.3 on page 11, and the outcoming parameters (v_p, K^{trans} and k_{ep}) can be used to evaluate the perfusion.

A way to achieve the curves is starting from Eqn. 2.3 on page 25 rewritten in terms of relaxation rate

$$R_1(t) - R_1(0) = r_1 C_{CA}(t) \tag{3.1}$$

where $R_1(t)$ is the longitudinal relaxation rate ($1/T_1$) at time t after contrast agent (CA) injection, $R_1(0)$ is the longitudinal relaxation rate before the injection of CA, r_1 is the relaxivity of CA and is a constant within a given environment, $C_{CA}(t)$ is the CA concentration at time t after the injection. Assuming that r_1 is constant in the different tissues examined (compartments), the Eqn. 3.1 can be rewritten as follows

$$\Delta R_1(t) = R_1(t) - R_1(0) \tag{3.2}$$

where the parameter $\Delta R_1(t)$ is directly proportional to the CA concentration in the tissue [20, 21]. By measuring the relaxation rates, before and after injection of CA, see section 2.3 on page 25, we can finally build the *time-concentration curves of Gadolinium*. From Eqn. 3.1 it is quite clear that we need to measure the T_1 relaxation time before and after CA injection. In this chapter we provide a short description of the materials used to perform the measurements, and an exhaustive description of the measurements of T_1 pre and post contrast with particular attention to the problems we needed to fix. The sequences described in this chapter, in order to carry out the measurement of T_1, are the main component of the imaging protocol.

3.1 Setup

All the experiments were performed on a GE Medical System (manufacturer's model name GENESIS_SIGNA) magnetic resonance scanner operating at 1.5 Tesla.

3.1.1 Surface coil and non-uniformity sources

As coil was used a quadrature phased array coil, in other words the coil usually used to image large field of view (FOV) as in the case of spine imaging. A phased array coil is essentially a number of overlapping coils (or elements), each with their own receiver detection circuitry. The term phased array comes from radar and is a bit confusing (where phase shift techniques are used in beam steering). A more appropriate name should be multi coil array. They are used to increase the surface area acquired whilst maintaining the SNR obtainable with a single surface coil. The acquisition in each coil (element) takes place simultaneously too, and so no increase in acquisition time is necessary. The behavior of this coil changes in reason of the load applied, so to simulate a more realistic case, several objects filled of distilled water were placed on the coil and close to our own phantom, till to approximate the weight of the torso of a patient. The images acquired by means of surface coils suffer from the variation of sensitivity of coils themselves, from here arises an intensity non-uniformity [22]. Next it is a list of possible sources of non-uniformity:

1. Non-uniformity in the transmitter $\boldsymbol{B_1}$ field. It is well known that the field generated by a radio-frequency coil is not completely homogeneous. The $\boldsymbol{B_1}$ field inhomogeneities are attributed to rf amplifiers distortions, digitization of the rf pulse and rf geometry. This is generally small if a separate larger coil is used for excitation and the surface coil is used for receiving only.

2. The rf penetration effects. The skin depth effect may prevent the rf transmitter field from penetrating the object. The effect increases with frequency, size of the object and electrical conductivity of the object. There are two results: first, the flip angle is reduced at the center of the object compared with that at the edge, giving a reduced precessing magnetization; and second, the signal detected externally from this magnetization is reduced.

3. Dielectric standing wave effects. These effects arise when the size of the object approaches one-half wavelength of electromagnetic radiation in the material concerned.

4. Imperfections in the filter used to restrict the bandwidth of the signal before Fourier transformation in the read direction. These effects are seen as

alterations in intensity near the edge of the image in the read direction; they are generally small in modern systems, provided a digital filter is used.

5. Static field and gradient non-uniformity, if present, will produce voxels with nonuniform size in the object. Larger voxels will contain more spins and appear artificially bright; smaller voxels will appear dark. Over a region that is small compared with the size of the gradient coils, this effect can be ignored. However, for a large FOV, as used for the spinal imaging, the effect can be significant.

To overcome the consequences of these effects on the images, manufacturers provide dedicated tools which correct for the non-uniformity, in our own case the SCIC (Surface Coil Inhomogeneity Correction) was provided, which consists of an algorithm GE proprietary, no documentation is released.

3.1.2 The phantom

The phantom utilized consisted of eight vials containing water doped with Gadolinium DTPA, more exactly Bracco's ProHance® (gadoteridol) was used, which is an MRI contrast medium with an established track record for imaging the brain, spine and surrounding tissues to improve visualization of lesions with abnormal vascularity, including primary and metastatic tumors. The T_1 values were in the range of 200 ms to 2700 ms. Before to be imaged the phantom was placed in a basket filled of water in order to avoid artifacts connected to the diamagnetic susceptibility. The vials were locked to the support by means of adhesive tape, this was necessary because the sound waves developed by coil make the vial vibrate, some artifacts should arise from these vibrations.

3.1.3 Processing tools

All processing has been carried out by means of free software and software made in house based on open source libraries. Next it is a list of free software used and their field of application:

- Medcon is principally used to convert data from DICOM format to Analyze format.

- ImageJ, a public domain Java image processing program, is used whenever it is necessary visualize the images and/or the maps, draw ROI, perform first and second order statistical analysis on the data extracted by means of the ROI.

- Mricro is essentially used to overlap images, with the objective of performing visual inspection before and after the co-registration is accomplished.

- GNUPLOT is widely utilized to plot data and, perform fitting of data collected from ROI.

The free libraries used in this work are: CERNLIB and Insight ToolKit (ITK), the code made in house is principally developed in $C++$ and Fortran90 languages.

The CERN Program Library is a large collection of general purpose programs maintained and offered in both source and object code form on the CERN central computers. Most of these programs were developed at CERN and are therefore oriented towards the needs of a physics research laboratory. Nearly all, however, are of a general mathematical or data-handling nature, applicable to a wide range of problems. The library contains several thousand subroutines and complete programs which are grouped together by logical affiliation into several hundred program packages. 80% of the programs are written in FORTRAN and the remainder in assembly code, or C usually with a FORTRAN version also available.

Insight Segmentation and Registration Toolkit (ITK) is an open-source software system to support the Visible Human Project. Currently under active development, ITK employs leading-edge segmentation and registration algorithms in two, three, and more dimensions. The Insight Toolkit was developed by six principal organizations, three commercial (Kitware, GE Corporate R&D, and Insightful) and three academic (UNC Chapel Hill, University of Utah, and University of Pennsylvania). Additional team members include Harvard Brigham & Women's Hospital, University of Pittsburgh, and Columbia University.

3.2 The measurement of reference T_1

The measurement of the reference T_1 of each tube in the phantom was carried out as first experiment. A nine points inversion recovery sequence with T_I equal to 50, 100, 200, 400, 600, 1000, 1500, 3000 and, 4000 ms was performed with constant receiver gain, $T_E = 9$ ms, $T_R = 4080$ ms, flip angle 90°, 160×256 image matrix interpolated to 256×256 and slice thickness 4 mm. This sequence lasts roughly one and half a hour, in fact each point of inversion recovery is long a time given by the product of number of phase encoding steps (in this case 160) and the repetition time (in this case $T_R = 4080$), this product is approximately eleven minutes. The phantom was scanned in coronal plane, i.e. the plane orthogonal to tubes. Mean signal values and standard deviations were obtained by evaluating a circular region of interest (ROI) drawn manually on each vial (97 pixel). The short T_I combined to the linear acquisition of the k-space can explain the fact that the initial magnetization is shorter than the magnetization at thermal equilibrium (magnetization at higher T_I), in other words, because the T_I before the minimum of the signal intensity are shorter than the T_1, this makes the magnetization reach a steady state different from that at thermal equilibrium, see figure 3.1 on page 46. This is the reason why the choice of Eqn. 3.3 on the facing page instead

of Eqn. 2.81 on page 39 was made to carry out the fitting. The T_1 values were, then, obtained from the equation

$$M_{\perp}(T_I) = \mid A - 2Be^{-T_I/T_1} \mid \tag{3.3}$$

by performing a nonlinear three parameters least squares fit based on the Levenberg Marquardt method of the experimental data as a function of delay time T_I, see appendix A on page 69. Such a method is already implemented in GNUPLOT. This function is more useful in measuring the T_1 with respect a two parameters function because the third parameters can account of the difference between the initial magnetization and the magnetization at the thermal equilibrium. The quantity $A - 2B$ is exactly the magnetization at the steady state and the parameter A is the magnetization at the thermal equilibrium. To check the fitting quality we look at the coefficient of determination R^2 see appendix B on page 73.

Once T_1 was measured for each vial, these values were used as reference for the next experiments. We report the T_1 measured by inversion recovery in table 3.1, for each value we report the standard error, for all the tubes was found $R^2 = 0.99$.

Sometimes the fitting was not converging, to overcome this shortcoming we needed to adjust the initial guess, necessary to perform non linear least square minimization, until convergence was achieved.

[Gd] mM	T_1 ms
0	2651 ± 36
0.025	2009 ± 22
0.05	1589 ± 23
0.1	1357 ± 13
0.125	1099 ± 18
0.25	743 ± 7
0.5	532 ± 4
1	208 ± 2

Table 3.1: The T_1 measured by means of Inversion Recovery are reported, for each value the standard error is reported, for all the tubes was found $R^2 = 0.99$. The higher concentration of CA, the shorter T_1.

3.3 Pre-contrast $T1$ measurement

A way to generate a computed T_1 map, potentially with less scanning time than required for conventional saturation recovery and inversion recovery methods is the *variable flip angle* sequence [21, 23, 24, 25]. The equation predicting the

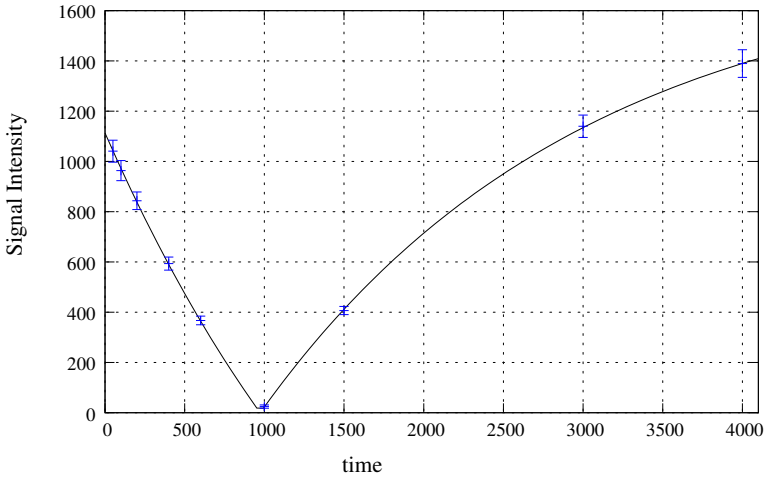

Figure 3.1: Plot of signal amplitude vs inversion time. For each point is depicted the mean signal intensity and, the standard deviation as well. The inversion time are reported, in units of ms, on the x axis whereas the signal intensity is reported on the y axis, no units.

signal intensity is

$$S(\alpha) = k\rho \frac{(1 - e^{-T_R/T_1}) \sin \alpha}{1 - e^{-T_R/T_1} \cos \alpha} \tag{3.4}$$

where k is a constant which takes into account the receiver gain, ρ is the proton density, α is the flip angle, T_R is the repetition time and T_1 is the relaxation time; here we made the approximation $T_E \ll T_2^*$, see Eqn. 2.79 on page 37. By acquiring several images at different flip angles but at same T_R and T_E one can obtain maps of T_1 by performing a non linear least squares fit on the images as function of flip angle. A 2D Fourier acquired at steady state (FAST) spoiled gradient (SPGR) gradient recalled echo (GRE) sequence was used in order to acquire the images being utilized to obtain the T_1 *pre-contrast* maps, from now onward we will refer (improperly) to this sequence as *variable flip angle acquisition*.

The necessity to be fast dictates the choice of a short T_R (50 ms) and, the 2D coverage of k-space as well, see section 2.5.2 on page 32, T_E was set at minimum (1.43 ms) to make negligible the factor e^{-T_E/T_2^*}, 160×256 image matrix. Compared with the sequence used in section 3.2 on page 44 this sequence lasts shorter time, in fact the time necessary in order to acquire an entire slab of eight slices is found by the product of *number of phase encoding* and T_R and, given the choice of $T_R = 50$ ms and, 160 phase encoding this product is 8 s, normally this sequence lasts more or less 30 s, we have to take into account the time necessary for the technicians to set the sequence. Furthermore the maximum time requested by a variable flip angle depends on the number of flip angles being acquired, generally few, this makes appealing the variable flip angle whenever it is necessary to measure T_1 without time consuming. Since the chosen T_R is

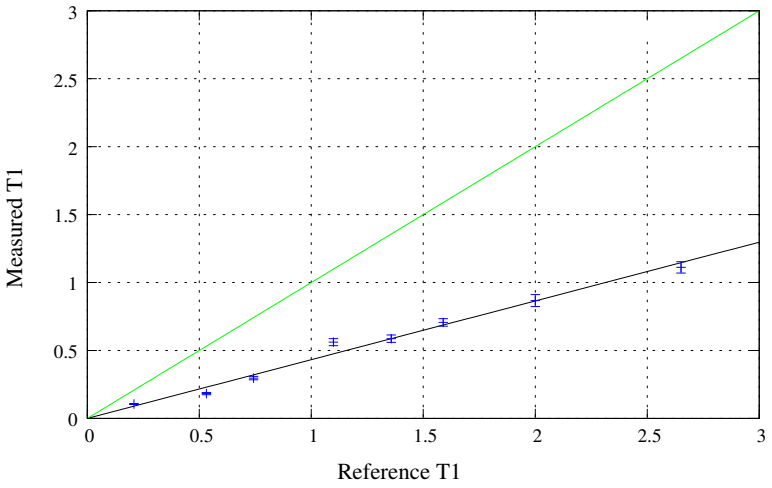

Figure 3.2: The T_1 measured by means of variable flip angle are depicted, the reference T_1, in units of s, are reported on the x-axis, whereas the measured T_1 are reported on the y-axis, in units of s as well. The T_1 estimated by variable flip angle fit a straight line (R^2=0.98) whose slope is different from that of reference. A calibration it is necessary to make the estimated T_1 be close to the reference T_1.

not enough long to allow the magnetization to recover the thermal equilibrium, a spoiling was applied before each rf pulse, see section 2.5.5 on page 37.

Dataset were acquired with nominal flip angle, time after time, equal to $10°, 13°, 15°, 18°, 20°, 23°, 25°, 28°, 30°, 35°, 40°, 45°, 50°, 60°, 70°$. Even in this case T_1 were estimated by performing a two parameters least squares fit based on the Levenberg Marquardt, see appendix A on page 69, method of the experimental data as a function of flip angle. It was found that the T_1 measured by using fifteen flip angles fit a straight line (R^2=0.98), but compared with the T_1 of reference, i.e. those measured by using the inversion recovery, are not exactly equivalent, see the figure 3.2. Therefore, in order to recover the real T_1, it's necessary to divide each estimated T_1 by the slope of the straight line fitted by T_1 estimated by using the variable flip angle.

Next two subsections describe the two tests carried out in order to check the goodness of the SCIC and make a choice of an ensemble of few flip angles to perform the variable flip angle.

3.3.1 Nonuniformity correction

Usually the 3D imaging of the spine is performed on the sagittal plane, along this plane the inhomogeneities are more manifest, so to be more realistic, the phantom was scanned in the sagittal plane, i.e. the plane parallel to the tubes. These images are then processed in order to measure pixel by pixel the T_1 of

the phantom. The picture 3.3 on the next page shows the same slice of the phantom in sagittal plane with and without SCIC application (right and left respectively), a linear plot was used to explain the difference between the images corrected and not corrected for the inhomogeneity; they are useful to see the considerable difference in case the images are corrected by SCIC or not. In absence of correction for the inhomogeneity the signal intensity decreases, as a function of distance from the coil, more rapidly than the case in which the correction is applied. The same sort of analysis was carried out on the T_1 map obtained by starting from images where the SCIC was applied and images where the SCIC was not applied.

As manifest from figure 3.4 on page 50 the SCIC can help to partially recover the homogeneity. The linear plots are traced along tube filled of homogeneous solution, in ideal conditions we should expect to see a horizontal line, but this does not happen because of inhomogeneities already discussed. Better results can be reached by means of the SCIC. We found that the T_1 measured by means of variable flip angle, but without application of SCIC, fit a straight line ($R^2 = 0.98$), but compared with the T_1 of reference, i.e. those measured by using the inversion recovery, are not exactly equivalent. Whereas in the case of map obtained starting from SCIC correction was found that the T_1 still fit a straight line ($R^2 = 0.94$), a calibration is necessary even in this case to recover the reference values.

3.3.2 Flip angles optimization

Another task was finding a set of flip angle whose performance in measuring the T_1 is comparable with that of a larger set of flip angle. This was done with the aim of shortening the time taken by variable flip angle acquisition, since for each patient we have only ten minutes the shorter variable flip angle the longer dynamic acquisition can be.

Taken into account that acquiring a single flip angle takes 30 s and, that normally the dynamic acquisition lasts eight minutes we have time enough to acquire at least five times the 2D FAST SPGR at different flip angles.

The choice of flip angle was made by means of indices of *accuracy* and *precision*. The *index of accuracy* i_a has been defined as:

$$i_a = \frac{1}{N} \sum_{i}^{N} \frac{| T1_i^{\text{ref}} - T1_i^{\text{measured}} |}{T1_i^{\text{ref}}} \tag{3.5}$$

where N is the maximum number of vials in the phantom, $T1_i^{\text{ref}}$ is the T_1 reference value of ith vial, see section 3.2 on page 44, so the smaller index the better accuracy. Similarly the *index of precision* i_p has been defined as:

$$i_p = \frac{1}{N} \sum_{i}^{N} \frac{\text{stdv}_i^{\text{measured}}}{T1_i^{\text{measured}}} \tag{3.6}$$

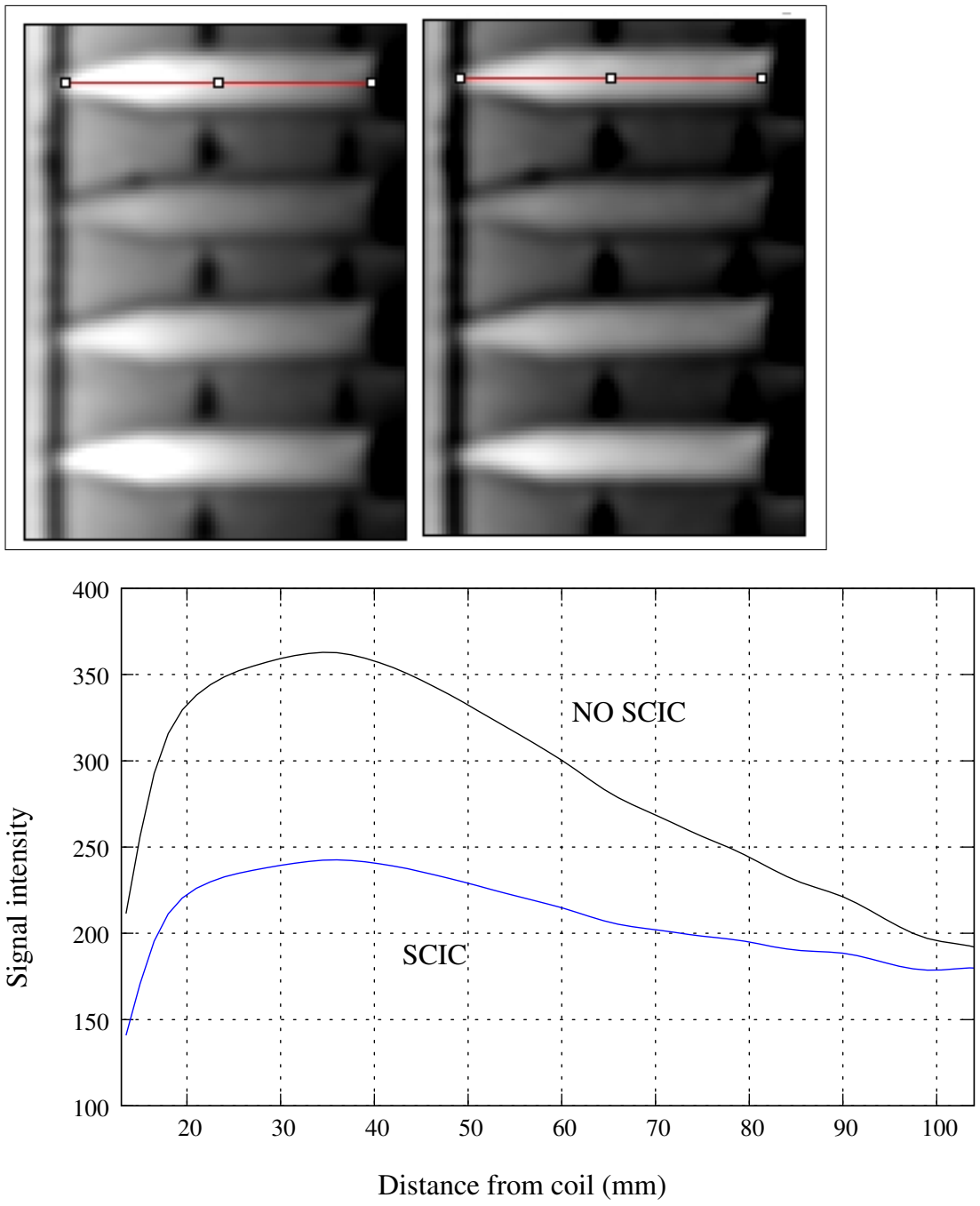

Figure 3.3: The same slice of the phantom in sagittal plane with and without SCIC application (right and left respectively). A linear plot (bottom) was used to show the difference between the images corrected and not corrected for the inhomogeneity. In absence of correction for the inhomogeneity the signal intensity decreases, as a function of distance from the coil, more rapidly than the case in which the correction is applied.

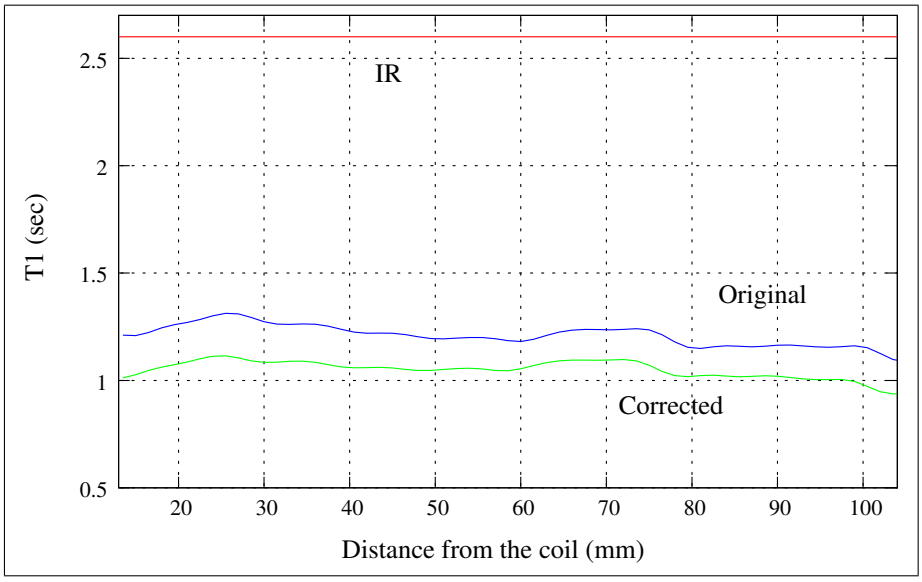

Figure 3.4: Linear plots traced on the maps of T_1. Each plot shows the difference between the T_1 measured from images where the SCIC was applied and images where the SCIC was not applied.

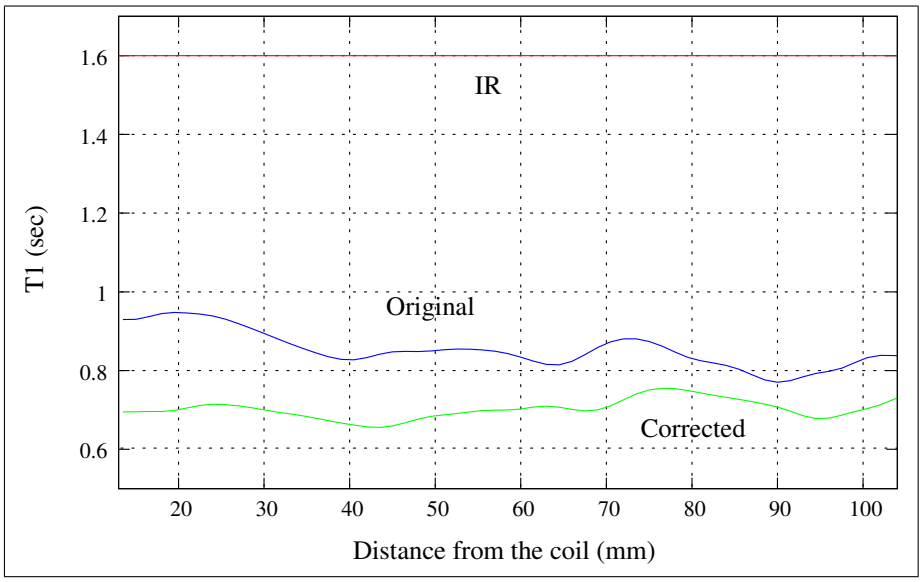

where stdv is the standard deviation (or better the standard error) of the parameter returned by GNUPLOT [26]. Next it is described the way we used to choose the five flip angles.

1. For each tube in the phantom, mean signal intensity and standard deviation, measured by manually drawing a circular ROI on the tube, were collected. This was done for all the fifteen flip angles.

2. All the possible combinations (3003) of arranging any five flip angles from the ensemble of fifteen flip angles were generated for each tube and, the T_1 and the standard error related to each combination were calculated.

3. The formulas 3.5 on page 48 and 3.6 on page 48 are finally used to evaluate the indices on which the choice of flip angle was done.

The values of precision, found for all the combinations, range from 0.02% up to 2%, apart some spikes. The combinations with high flip angles show the worst value of precision, this is due to the fact that the SNR decreases at high flip angle. The found mean value of accuracy is 29% with a standard deviation of 6%. Again, the combinations including high flip angles show the worst values of accuracy. The ensemble $\{15°, 18°, 20°, 23°, 35°\}$ is the set of flip angle chosen on the basis of accuracy and precision. We found that the combination of flip angle with good precision not necessarily has the best value of accuracy, so it was necessary to find a trade off between accuracy and precision, in particular the cited ensemble shows good precision (5%) and not so bad accuracy (25%). The performance of this set of flip angle in measuring the T_1 is comparable with that of fifteen flip angles. The sum over the square difference between the T_1 estimated from the full set of flip angles and the T_1 evaluated by means of the chosen five flip angle is very small, only 1.6×10^{-3}.

3.4 Post contrast T_1 measurement

The basis of DCE is acquiring frames at a temporal resolution good to carry out the fitting of the chosen model in order to describe the transport of Gadolinium in the tissues. The way to increase the temporal resolution should be using a 2D imaging, but as it is known, see 2.5.3 on page 32, this method cannot acquire all the volume of the tumor because of the gap between the slices, so the net result should be have high temporal resolution in change of poor spatial information that can lead to misleading results. The 3D imaging in this case is strictly necessary. The dynamic acquisition of data was performed by means of a 3D GRE SPGR at fixed flip angle and T_R, the equation predicting the signal intensity is still the 3.4 on page 46; before the injection of contrast agent three frames are acquired as baseline, then the dynamic acquisition starts simultaneously with

contrast injection, the acquisition lasts more or less eight minutes, during this time $36 \div 38$ frames are acquired with temporal resolution of 11 seconds.

Starting from Eqn. 3.4 on page 46 we can measure the T_1 post-contrast by the ratio of signal post-contrast and the average baseline signal. We indicate the baseline signal with S^{pre}, whereas the post-contrast signal with S^{post}. The ratio is

$$\begin{aligned} \frac{S^{\text{post}}}{S^{\text{pre}}} &= \frac{k\rho(1-e^{-T_R/T_1^{\text{pre}}})\sin\theta}{(1-\cos\theta e^{-T_R/T_1^{\text{pre}}})} \frac{(1-\cos\theta e^{-T_R/T_1^{\text{post}}})}{k\rho(1-e^{-T_R/T_1^{\text{post}}})\sin\theta} \\ &= \frac{(1-e^{-T_R/T_1^{\text{pre}}})}{(1-\cos\theta e^{-T_R/T_1^{\text{pre}}})} \frac{(1-\cos\theta e^{-T_R/T_1^{\text{post}}})}{(1-e^{-T_R/T_1^{\text{post}}})} \end{aligned} \tag{3.7}$$

where T_1^{pre} is the relaxation time in absence of Gadolinium, we use here the T_1 measured as illustrated in section 3.3 on page 45. The only unknown in Eqn. 3.7 is T_1^{post}, we can calculate it from following expression (achieved by manipulating the Eqn. 3.7)

$$T_1^{\text{post}} = T_R \ln \frac{1-A}{1-A\cos\theta} \tag{3.8}$$

where

$$A = \frac{S^{\text{post}}}{S^{\text{pre}}} \frac{1-e^{-T_R/T_1^{\text{pre}}}}{1-e^{-T_R/T_1^{\text{pre}}}\cos\theta} \tag{3.9}$$

The goodness of the sequence in measuring the T_1 was checked by means of indices of accuracy and precision, see Eqn. 3.5 on page 48 and Eqn. 3.6 on page 48. The usual phantom was scanned in sagittal plane with 3D dynamic sequence, the images obtained were smoothed, then were exploited in order to perform the test. As evident from Eqn. 3.9, to measure the T_1^{post} of each tube it is necessary a S^{pre} and a T_1^{pre} as well, these two values are provided by fixing a reference tube whose T_1 is already known from the IR experiment and, whose S^{pre} can be measured by means of an ROI. Once these two values are provided, a map of T_1^{post} is obtained by means of software made in house which implements the Eqn. 3.7, these T_1^{post} maps are then used in order to extract the T_1^{post} of the other tubes by means of ROI. The figure 3.5 on the facing page shows how the T_1^{post} measured by this sequence are close to the reference T_1. To keep a reasonable temporal resolution the T_R was kept at 5.3 ms, image matrix 160×256 interpolated to 256×256 and, slice thickness 4 mm, but several tests were carried out with the aim of optimizing the choice of flip angle and, the k-space coverage modality as well, on the basis of accuracy and precision. Summarized in the table 3.2 on the next page and 3.3 on the facing page are the values of accuracy and precision at different flip angles and k-space covering, the flip angle chosen is 15°, while as k-space covering modality was selected the linear covering. The flip angle 15° was chosen because it shows the best values of accuracy and precision with respect the others, independently from the k-space coverage; whereas the choice of linear

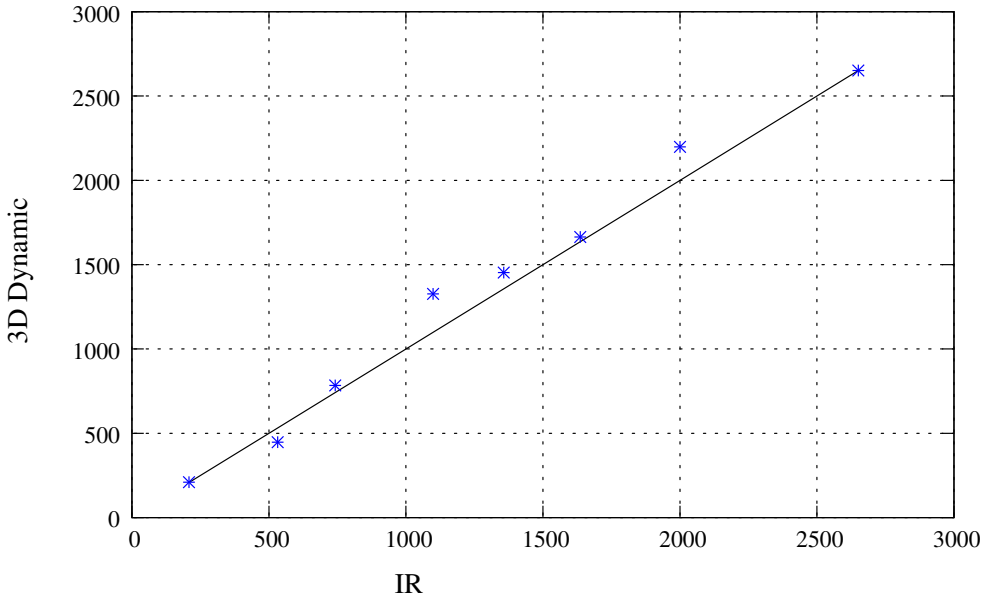

Figure 3.5: The T_1 measured by means of the 3D Dynamic acquisition are depicted. The T_1 measured by means of this sequence (stars) are very close to the reference T_1 (straight line).

k-space coverage	Flip Angle (degree)		
	12	15	18
linear	0.121	0.101	0.109
centric	0.224	0.126	0.134
spiralcentric	0.173	0.107	0.145

Table 3.2: Index of accuracy

k-space coverage	Flip Angle (degree)		
	12	15	18
linear	0.161	0.159	0.163
centric	0.139	0.127	0.148
spiralcentric	0.161	0.154	0.179

Table 3.3: Index of precision

k-space coverage was made on the basis of reasons shown in the section 3.5 on page 54.

3.5 Aortic blood T_1

The discovery of the nuclear magnetic resonance (NMR) phenomenon by Purcell and Bloch was rapidly followed by the first observations on the dependence of NMR from flow and motion [27]. The first observation of what is now referred to as *time of flight* (TOF) effect was by Surynan who noted that T_1 of flowing water was effectively shorter than the T_1 of stationary water. The difference can be attributed to the fact that when stationary, the spins would be saturated by the radiofrequency excitation but, when flowing, fresh spins with full magnetization would replace the stationary spins thereby increasing the signal. The degree of signal enhancement depends upon the velocity of the blood v, the slice thickness z and the interval between radiofrequency pulses T_R. If the blood is stationary ($v = 0$) then the blood within the slice receives two rf pulses at t and $t + T_R$, partially saturating the spins. If the blood is moving at a velocity such that $v = \frac{1}{2}(z/T_R)$ then half spins within the slice will be replaced with unsaturated spins, i.e. those with no prior rf history, during T_R. The result is an increase in the vascular signal. If the blood velocity is such that $v = z/T_R$ then all the spins within the slice will be replaced with unsaturated spins during T_R yielding maximal vascular signal. Any velocity above this threshold will not increase enhancement further. It is clear, then, that T_1 depends upon the flow velocity and this is a source of non-uniformity that can distort the measures. There is an extra effect to keep in mind, given a short T_R (strictly inferior to the T_1 of the blood) the magnetization cannot recover the thermal equilibrium but at most can reach a lower steady state. Next is described the method to calculate the magnetization after n rf pulses. We consider a gradient echo sequence such as that in the section 2.5.5 on page 34. Beginning with longitudinal magnetization M_0, the longitudinal magnetization after the nth T_R interval is

$$\begin{aligned} M_n &= M_{n-1}\cos\theta + (1 - e^{-T_R/T_1})(M_0 - M_{n-1}\cos\theta) \\ &= (1 - e^{-T_R/T_1})M_0 + KM_{n-1} \end{aligned} \tag{3.10}$$

where $K = \cos\theta e^{-T_R/T_1}$. Writing as a sequence we have

$$\begin{aligned} M_n &= (1 - e^{-T_R/T_1})M_0(1 + K + K^2 + \ldots + K^n) + K^n e^{-T_R/T_1} M_0 \\ &= (1 - e^{-T_R/T_1})M_0 \frac{1 - K^{n+1}}{1 - K} + K^n e^{-T_R/T_1} M_0 \end{aligned} \tag{3.11}$$

Since $K < 1$,

$$M_n \to \frac{(1 - e^{-T_R/T_1})M_0}{(1 - K)} \qquad n \to \infty. \tag{3.12}$$

The following quantity

$$f \equiv \left(\frac{M_n - M_\infty}{M_\infty}\right) \tag{3.13}$$

where M_∞ is the magnetization at steady state, give us the idea of how far from the steady state is the magnetization after n rf pulses; the smaller fraction f the closer to the steady state is the magnetization in the specimen. The number of pulses necessary for the sample to reach the steady state depends upon the flip angle, see section 2.1.4 on page 22, T_R and T_1.

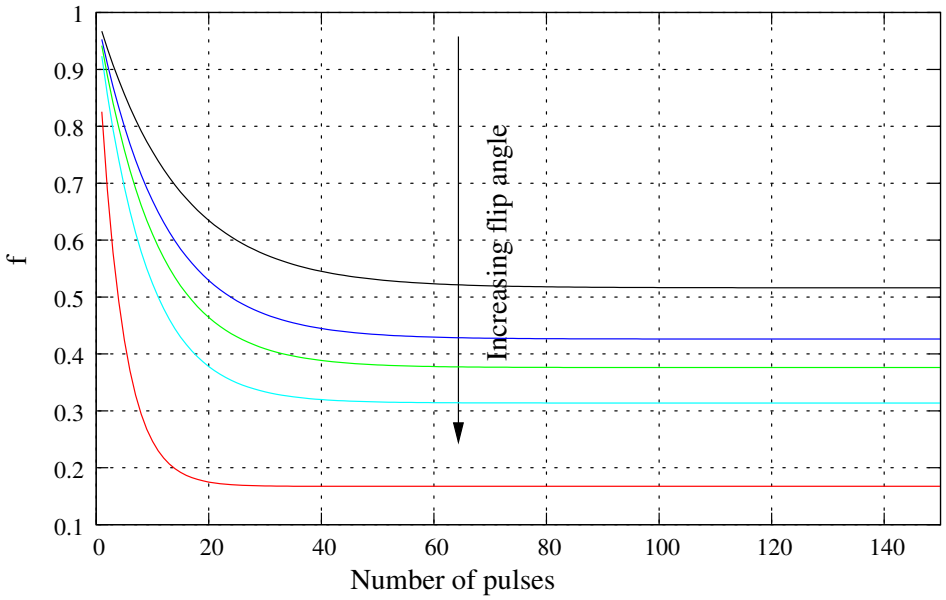

Figure 3.6: The course of f, pulse after pulse. The T_R is kept fixed at 50 ms, T_1 is equal to 1400 ms whereas the flip angle FA=15°,18°,20°,23°,35°. It is shown the dependence of f from the T_R.

Figures 3.6 and 3.7 on the next page show the behavior of the magnetization when the time to recover thermal equilibrium is short, on the x-axis is reported the number of pulses whereas on the y-axis is reported the f value given by the Eqn. 3.13. Similarly, for T_R, T_1 constant, the time needed to reach the steady state decreases as flip angle values increase, while, at fixed T_R and flip angle values, this time increases with T_1.

In order to know how many pulses a volume of blood can undergo while it is in the excitation field we need to know its velocity. The average aortic blood velocity for a subject at rest can be estimated as follows: the stroke volume (SV) is usually in the range $60 - 100$ ml and the heart rate $60 - 80$ beats/min, for a cardiac output of $4 - 8$ l/min, the mean diameter of the descending aorta is 2.5 cm. Next equation can be used in order to calculate the blood velocity:

$$v_{ba} = \frac{SV \times HR}{60 \times \pi r^2} \tag{3.14}$$

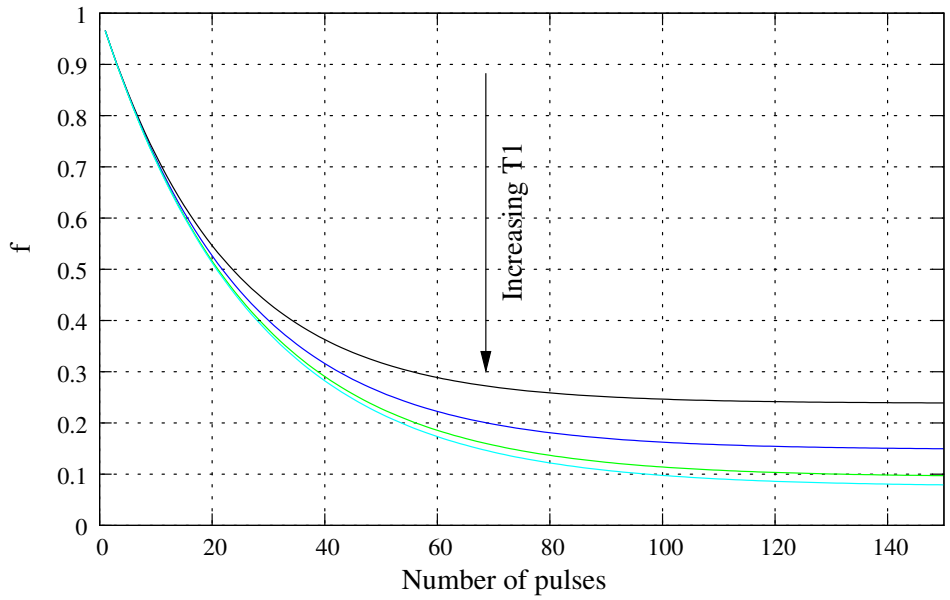

Figure 3.7: The course of f, pulse after pulse. The T_R is kept fixed at 5.3 ms, the flip angle is equal to 15° whereas the T_1=500,900,1500,1900 ms. It is shown the dependence of f from the T_1.

where SV is the stroke volume in units of ml, HR is the heart rate in units of beats a minute, r is the radius of the descendent aorta in units of cm. It can be found that the blood velocity is in the range $12 \div 27$ cm/s. Once the blood velocity is known, we can calculate the number of rf pulses that the blood undergoes while is traveling across the excitation field. We suppose that the irradiation field is 20 cm long, so a well defined volume of blood, given a blood velocity of 19 cm/s, will stay in the field of excitation only for 1.05 s and it will undergo $1.05/T_R$ pulses. Considering the sequences that we use in order to acquire the images pre and post contrast injection, the blood undergoes 198 pulses (1.05 s/0.0053 s) in the case of 3D imaging whereas just 21 pulses (1.05 s / 0.05 s) in case of 2D imaging. Now, by means of Eqn. 3.13 on page 54 and taken into account that the average relaxation time of a blood sample at 1.5 T is 1500 ms [28] we can calculate the fraction of steady state reached.

The variable flip angle with $T_R = 50$ ms is not a good candidate to measure the T_1 of non static tissues, the magnetization is still far from the steady state and for the same T_1 the system reaches different fraction of steady state, see table 3.4 on the next page, at different flip angles; this means that there should be some inhomogeneities which can distort the measurement of T_1. For this reason the T_1 pre contrast of the blood in not measured by using the variable flip angle but, rather, it's used an average value known from literature [28].

On the contrary, the 3D GRE SPGR with $T_R = 5.3$ ms shows better performance in measurement of blood T_1, in fact the fraction f is only 0.5%. A way

T_R ms	flip angle (degree)	f %
50	15	24
50	18	25
50	20	24
50	23	20
50	35	4

Table 3.4: The fraction of steady state reached by a volume of blood for different flip angle and, in case of 2D imaging.

to improve the fraction of steady state is to select a *linear* k-space coverage, see section 2.5 on page 27, it consists in sampling the Fourier-domain row by row starting from the left corner at bottom and ending at the top left corner, in this way first are acquired high frequencies components, then, when passing across the center of Fourier-domain are acquired low frequencies components. The information carried by the blood is located in the middle of Fourier-domain, this means that the blood, before to be imaged, takes at least half the pulses which are necessary to cover all the k-space, these extra pulses make the blood reach the steady state in a shorter time. In other words we expect to see the signal reaching a plateau, in order to verify this hypothesis we drew several circular ROIs over the descendent aorta, mean signal intensity and standard deviation were extracted all over the descendent aorta, in order to follow the blood flow in the irradiation field. In figure 3.8 on the next page is depicted the course of signal intensity along the segment of descendent aorta before (black line) and after contrast agent injection, on the x-axis there is the position of blood sample along the aorta (starting from the top going to the bottom) whereas on the y-axis there is the blood sample signal intensity; in order to avoid partial volume effect the stack of images acquired in the sagittal plane was re-sliced in the axial plane, in this way the ROIs were drew on the cross section of the aorta (see figure 3.9 on the following page).

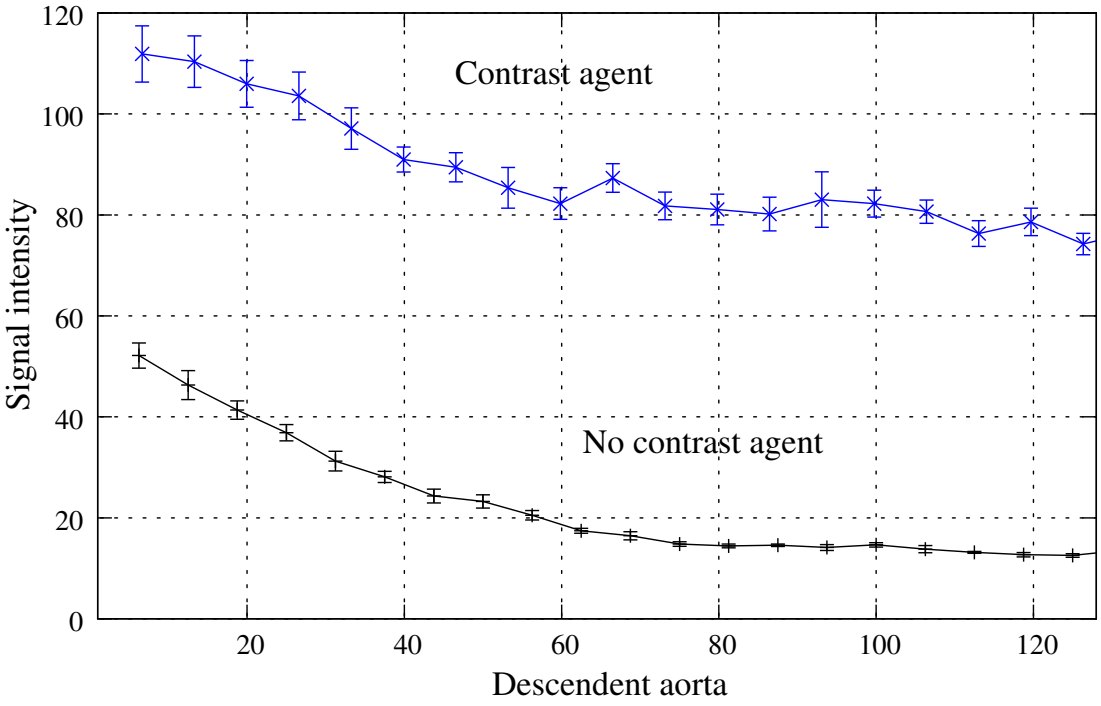

Figure 3.8: The curves show the blood's course signal intensity, while the blood is in the irradiation field. As expected the blood reaches a steady state (plateau), usually the signal intensity necessary to estimate the AIF is measured by drawing the ROI where the blood's signal intensity is at the steady state in order to avoid flow artifact.

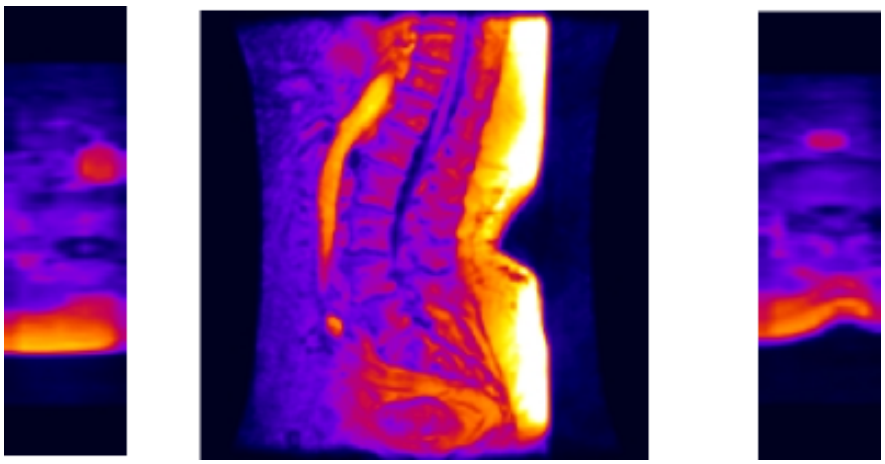

Figure 3.9: An example of reslicing. The images in the middle is acquired in the sagittal plane, whereas the two images on the side are resliced to the axial plane. The cross section of the aorta (top of the images on the side) it is visible.

Chapter 4

Data processing and first results

As already mentioned in the previous chapters, the tumor perfusion can be quantitatively evaluated by means of the parameters introduced in the section 1.3 on page 11. In order to obtain a quantitative estimate of these parameters it is necessary to fit the model to the experimental concentrations, in this case $\Delta R_1(t)$, acquired as explained in the chapter 3. The processing of the images can be carried out pixel by pixel or more simply on a single $\Delta R_1(t)$ curve, see Eqn. 3.2 on page 41, obtained by drawing an ROI on a lesion of interest. This chapter is dedicated to show the way to achieve the parameters from the fitting of $\Delta R_1(t)$ curve. The main steps of this processing tools are as follows.

1. Convert the images from DICOM format to Analyze format.
2. Blurr the images.
3. Perform the registration of images acquired by 2D imaging to images acquired by 3D imaging.
4. Calculate T_1 pre and post contrast.
5. Compute $C_p(t)$.
6. Convert T_1 to $\Delta R_1(t)$.
7. Apply the fitting procedure to $\Delta R_1(t)$ and finally obtain the compartmental model parameters.

The native images format is not appropriate to be handled and the analyze format if preferable because the header informations are separated from the matrix of signal intensity, which makes easer dealing with images being processed.

Blurring is the traditional approach for removing noise from images. It is usually implemented in the form of a convolution with a kernel. The effect of blurring on the image spectrum is to attenuate high spatial frequencies. One of the most commonly used kernels is the Gaussian one; the convolution of the input

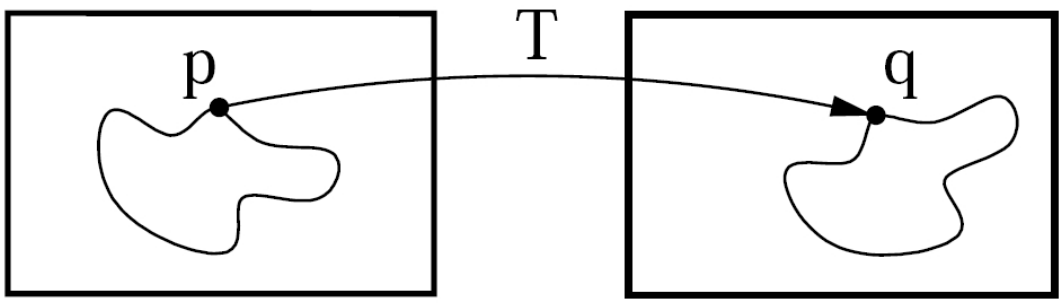

Figure 4.1: Image registration is the task of finding a spatial transform mapping on image into another.

image with a Gaussian kernel is computed by means of a class, i.e. some code which implements particular algorithms, provided by ITK (see section 3.1.3 on page 43). Here the class itk::DiscreteGaussianImageFilter was used in 2D and 3D by taking advantage of the separability of the Gaussian kernel. Usually a one-dimensional discretized Gaussian function is used and its size is extended until there are enough discrete points to ensure that a user-provided maximum error is not exceeded. Since the size of the kernel is unknown a priori, it is necessary to impose a limit to its growth, hence the user must thus provide a value to be the maximum admissible size of the kernel. Gaussian kernels in ITK are constructed so that smoothing and derivative operations commute before and after discretization. In other words, finite difference derivatives on an image I that has been smoothed by convolution with the Gaussian are equivalent to finite differences computed on I by convolving with a derivative of the Gaussian.

Registration is an essential step. As already discussed in the section 3.3 on page 45 the measurement of T_1 pre contrast is carried out by acquiring the images with 2D multisclice technique, whereas the T_1 post contrast is done by means of images acquired with 3D imaging. Usually the volumes acquired by means of 3D imaging differ from those acquired by 2D multislice imaging, see section 2.5.2 on page 32, thus the images acquired by the two modality are not exactly overlapping, while in this study the overlapping is required; if this condition is not satisfied Eqn. 3.7 on page 52 cannot be used. The registration can help to overcome this drawback. Image registration is the process of determining the spatial transform that maps points from one image to homologous points on a object in the second image. This concept is schematically represented in Figure 4.1. The basic input data to the registration process are two images: one is defined as the *fixed* image $f(\boldsymbol{X})$ and the other as the *moving* image $m(\boldsymbol{X})$. Registration is treated as an optimization problem with the goal of finding the spatial mapping that will bring the moving image into alignment with the fixed image. The *transform* component $T(\boldsymbol{X})$ represents the spatial mapping of points from the

fixed image space to points in the moving image space. Note that this definition is inverse to the usual view of image transformation. Using the inverse transform is typical in registration as it avoids the potential problems of *holes* with the forward transform. The *interpolator* is used to evaluate moving image intensity at non-grid positions, while the *metric* component $S(f, T(m))$ provides a measure of how well the fixed image is matched by the transformed moving image. This measure forms the quantitative criterion to be optimized by the *optimizer* over the search space defined by the parameters of the transform. More detailed informations about registration can be found in [29].

The fitting procedure used to obtain T_1 pre contrast and the parameters of the model (K^{trans}, v_p, k_{ep}), is, in general, as follows. Given a function $f : \Re^{k+1} \to \Re$, where k is the number of parameters to be found, a cost function is defined

$$F = \sum_{i=1}^{N} (f(p_1, p_2, \ldots, p_k, x_i) - d_i)^2 \tag{4.1}$$

where N is the number of experimental data, p_j is the jth parameter and, d_i is the ith element in the dataset. The k parameters are obtained by finding the minimum of F in the parameters space. The fitting procedure starts evaluating the value of F on the basis of an initial guess vector, i.e. a vector of reasonable parameters provided by the user, then step by step this vector is updated on the basis of the data returned by an *optimizer*. The optimizer has the role of finding the minimum of the function F in the search space. At each step the value of F is compared with a tolerance error . The fitting procedure ends as soon as F is below the tolerance error or a maximum number of steps is reached. On the last step the parameters are finally returned.

This algorithm has been implemented by house made code, based on MINUIT, the *optimizer* provided by the CERNLIB, see section 3.1.3 on page 43.

The $C_p(t)$ curve is evaluated by drawing an ROI (about 10 pixels) on the artery feeding the tumor in a place of the artery where the blood is at the steady state for the reasons already explained in section 3.5 on page 54; particular attention must be devoted to avoid effects of partial volume. In this work the descendent aorta was used because the foci are located on the spine. The plasma concentration has been sampled with the temporal resolution, given by 3D dynamic imaging, of eleven seconds. The signal intensity is then converted to $\Delta R_1(t)$ and fitted by a biexponential curve (see section 1.3 on page 11). Given the cardinal role of $C_p(t)$ in the Eqn. 1.5 on page 13, there may be benefits for the accuracy of derived kinetic parameters reducing noise on this curve; figure 4.2 on the following page shows both the sampled $C_p(t)$ and the fitted $C_p(t)$ (smoothed), the smoothed $C_p(t)$ is then passed to the model as AIF.

All this procedure can be performed on a single point (as in case of ROI analysis) or pixelwise; in case of ROI analysis, the ROI must be drawn before the point 4 in the preceding list of instructions. Generally the fitting is computa-

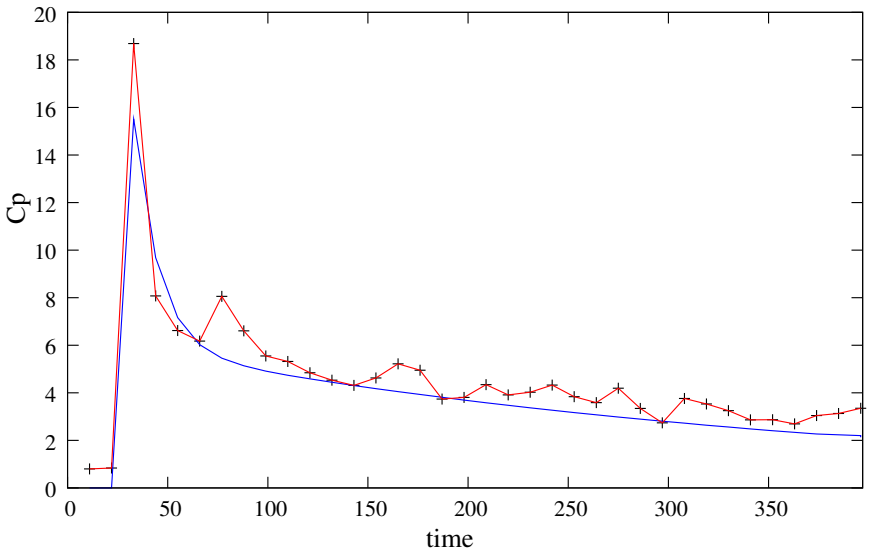

Figure 4.2: Temporal evolution of concentration of contrast agent in the aortic blood. The $C_p(t)$ curve is measured on a patient, while the smoothed curve is achieved by means of Eqn. 1.6 on page 13.

tionally very intensive, and in cases where many thousands of image pixels must be analyzed (as in case of pixelwise analysis), then online processing can become lengthy even with very fast processors. In this study the problem of keeping low the computational complexity was taken in consideration, a first way to attain this objective has been reducing the number of image pixels, being analyzed, by means of a mask, usually placed on the region occupied by the spine. Then starting from the results of Mark A. Horsfield and Bruno Morgan [30], the time request by fitting procedure was enormously shortened, at least ten fold. The first approach to fitting procedure was implementing the Eqn. 1.5 on page 13 iteratively, soon this procedure shown its limits: it is very slow. Best performances are shown by recursive implementation of the model used in this study. Let us consider the discrete equation of the chosen model

$$C_t(t) = v_p C_p(t) + K^{\text{trans}} \Delta\tau \sum_{i=1}^{t} C_p(t) e^{-k_{ep}(t-i)} \tag{4.2}$$

where $\Delta\tau$ stands for the discrete time interval. In the first implementation the $C_t(t)$ is obtained by means of two loops, the first contained in the second. These two loops have the same size, which makes the computational complexity be $O(n^2)$, where n is the size of the loop, usually this loop's size is related to the number of temporal frames acquired during the dynamic sequence. In the recursive implementation $C_t(t)$ is updated time after time by using the following formula:

$$C_t(t+1) = C_t(t) + U(t) \tag{4.3}$$

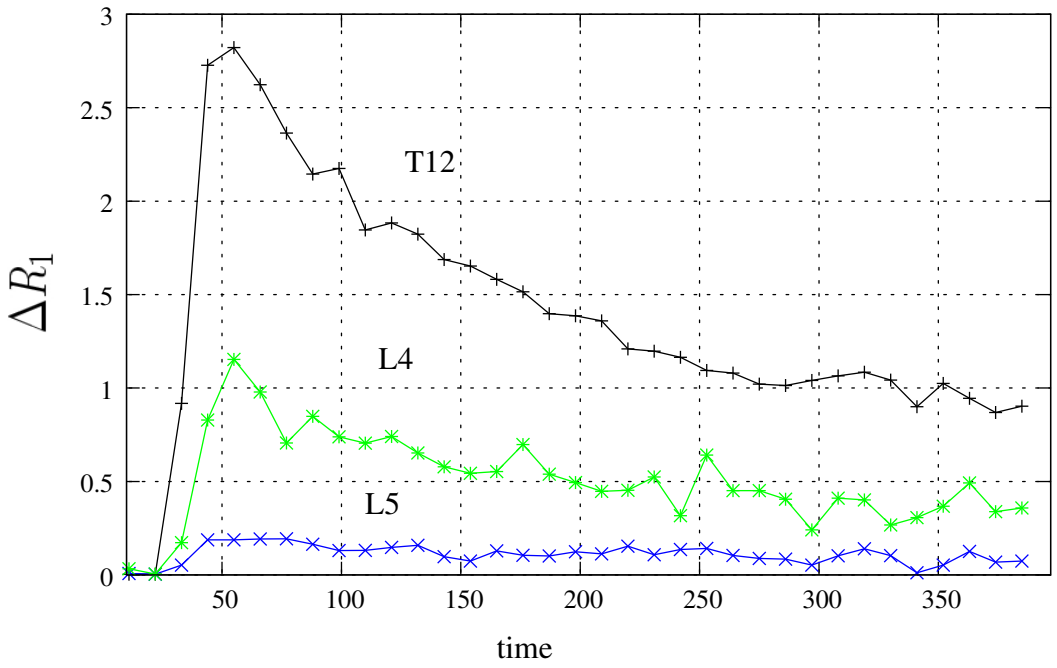

Figure 4.3: $\Delta R_1(t)$ measured on three vertebrae.

where $U(t)$ is the updating term. The computational cost of this formula is $O(n)$, this explains why the recursive implementation is faster than the iterative implementation.

4.1 First results

Typical $\Delta R_1(t)$ curves are depicted in figure 4.3; these curves are obtained by drawing a circular ROI on three different vertebrae of a patient with metastases from prostate cancer, these data refer to the baseline DCE-MRI acquisition. The ROI on the vertebra T12 has area 52 pixels whereas the ROI on the vertebrae L4 and L5 have area 37 pixel. The vertebra T12 has a lesion on the posterior part, the vertebra L4 is the control vertebra while the vertebra L5 shows low uptake of tracer due, probably, to necrosis. The lesion on the vertebra T12 shows rapid and high uptake of contrast agent and, rapid wash out as well, so we should expect to have huge values of K^{trans} and k_{ep} whereas the lesion on L5 vertebra should show short values of K^{trans} and k_{ep} (see section 1.3 on page 11).
As clear from the tables 4.1 on the following page the parameters K^{trans} and k_{ep} have values which make possible to distinguish between aggressive cancer and healthy tissues and necrotic tissues. Next tables show the time evolution of these parameters estimated on the same patient over a time interval of four months, the images acquired time after times are registrated to the images acquired during the baseline scan, this was done with the aim of performing the measurements on

Vertebra	v_p	K^{trans} min^{-1}	k_{ep} min^{-1}
T12	$< 10^{-4}$	0.0531 ± 0.0119	0.0567 ± 0.0096
L4	$< 10^{-4}$	0.0192 ± 0.0069	0.0428 ± 0.0041
L5	0.0008 ± 0.0017	0.0021 ± 0.0025	0.0199 ± 0.0172

Table 4.1: Parameters estimated from baseline acquisition. For each parameter the mean value and the standard deviation are reported.

the same voxels used to analyze the baseline. Each table reports the data related to one and only one vertebra, this way the time evolution of parameters should be analyzed easily.

v_p	K^{trans} min^{-1}	k_{ep} min^{-1}
$< 10^{-4}$	0.0162 ± 0.0030	0.0361 ± 0.0054
$< 10^{-4}$	0.0308 ± 0.0066	0.0524 ± 0.0064
0.0304 ± 0.0209	0.0237 ± 0.0073	0.0436 ± 0.0129

Table 4.2: Time evolution of parameters estimated on the vertebra T12, for each parameter the mean value and the standard deviation are reported.

v_p	K^{trans} min^{-1}	k_{ep} min^{-1}
$< 10^{-4}$	0.0095 ± 0.0027	0.0296 ± 0.0024
$< 10^{-4}$	$< 10^{-4}$	0.0182 ± 0.0038
0.0005 ± 0.0015	0.0032 ± 0.0007	0.0248 ± 0.0040

Table 4.3: Time evolution of parameters estimated on the vertebra L4, for each parameter the mean value and the standard deviation are reported.

v_p	K^{trans} min^{-1}	k_{ep} min^{-1}
0.0023 ± 0.0043	0.0031 ± 0.0017	0.0220 ± 0.0048
$< 10^{-4}$	$< 10^{-4}$	$< 10^{-4}$
0.0057 ± 0.0058	0.0025 ± 0.0012	0.0196 ± 0.0071

Table 4.4: Time evolution of parameters estimated on the vertebra L5, for each parameter the mean value and the standard deviation are reported.

The parameters of the vertebrae L4 and L5 are compromised during the third scan, second row of table 4.3 and 4.4, because one of the coils used didn't work

that day. However this data have no statistical significance, because related to a single patient, but some variations are manifest. According to the results of some simulations we found that aggressive tumors show huge values of K^{trans} and k_{ep} as well, whereas necrotic tissues show the shortest values of K^{trans} and k_{ep}. This behavior is observed among all the MRI scans performed on the same patient during a time interval of four months.

Chapter 5

Conclusions and future directions

In this thesis tools performing non invasive and quantitative analysis of tumor vascularization are developed, these tools exploit the leaks of tumor vessels jointly to the contrast agent. DCE-MRI is the technique used to image the angiogenesis, T_1-weighted images are acquired before, during and after contrast injection. Several tests are performed on phantoms and volunteers in order to optimize the sequence-parameters such as flip angle and k-space coverage; this optimized protocol is used to carry out the DCE-MRI on patients with metastases from breast and prostate cancer. From the images acquired in such a way, T_1-maps are then extracted and arranged to feed the model which describes the transport of contrast agent between the tissues. A bicompartmental (three parameters) model is exploited in order to quantitatively evaluate the tumor perfusion in patients undergoing antiangiogenic therapy. All the code devoted to performing the data processing is house made and tested, we are confident that the processing tools are robust and effective, several months were dedicated to testing them.

Some simulations are carried out in order to understand the role of each parameter in the model, so according to the results of these simulations we found that aggressive tumors show huge values of K^{trans} and k_{ep} as well, whereas necrotic tissues show the shortest values of K^{trans} and k_{ep}. This behavior is observed among all the MRI scans performed on the same patient during a time interval of four months, unfortunately one MRI scan failed because of a coil which did not work properly. In general the first results achieved show that we are able to distinguish between several sort of tumoral tissues. Maybe higher order statistics jointly to clustering (methods for grouping objects of similar kind into respective categories) may reveal more informations and help evaluating the follow-up, however performing statistical analysis of the data is beyond the objectives of this work; the main goal of this work has been developing and testing tools being utilized whenever a quantitative analysis of tumor perfusion is necessary.

Next steps will be rewrite all the code with object oriented language, such as C++, leaving definitively the CERNLIB library and passing to the GSL (Gnu Scientific Library). We want to make all these tools ease to be handled by tech-

nicians, especially the tool for the coregistration. Also we want to extend the quantitative analysis to primary breast tumor, the knowledges acquired on this work will be of help to perform tests on a new MRI scanner recently acquired by IRCC (Institute for Cancer Research and Treatment) in Turin.

Appendix A

Levenberg Marquardt algorithm

The Levenberg-Marquardt (LM) algorithm is the most widely used optimization algorithm. The problem for which the LM algorithm provides a solution is called *Nonlinear Least Squares Minimization*. This implies that the function to be minimized takes the following form:

$$f(\boldsymbol{x}) = \frac{1}{2}\sum_{j=1}^{m} r_j^2(\boldsymbol{x}) \tag{A.1}$$

where $\boldsymbol{x} = (x_1, x_2 \dots x_n)$, and each r_j is a function from $\Re^n$ to $\Re$. The r_j are referred to as a *residuals* and it is assumed that $m \geq n$. To make matter easier, f is represented as a *residual vector* $\boldsymbol{r} : \Re^n \rightarrow \Re^m$ defined by

$$\boldsymbol{r}(\boldsymbol{x}) = (r_1(\boldsymbol{x}), r_2(\boldsymbol{x}), \dots, r_m(\boldsymbol{x})) \tag{A.2}$$

Now, f can be rewritten as $f(\boldsymbol{x}) = \frac{1}{2} \parallel r(\boldsymbol{x}) \parallel^2$. The derivatives of f can be written using the Jacobian matrix $\boldsymbol{J}$ of $\boldsymbol{r}$ with respect to $\boldsymbol{x}$ defined as $\boldsymbol{J}(\boldsymbol{x}) = \frac{\delta r_j}{\delta x_i}$, $1 \leq j \leq m$, $1 \leq i \leq n$.

Let us first consider the linear case where every r_i function is linear. Here, the Jacobian is constant and we can represent r as a hyperplane through space, so that f is given by the quadratic $f(\boldsymbol{x}) = \parallel \boldsymbol{J}\boldsymbol{x} + \boldsymbol{r}(0) \parallel^2$. We get also $\nabla f(\boldsymbol{x}) = \boldsymbol{J}^\intercal(\boldsymbol{J}\boldsymbol{x}+\boldsymbol{r})$ and $\nabla^2 f(\boldsymbol{x}) = \boldsymbol{J}^\intercal\boldsymbol{J}$. Solving for the minimum by setting $\nabla f(\boldsymbol{x}) = 0$, we obtain $x_{min} = -(\boldsymbol{J}^\intercal\boldsymbol{J})^{-1}\boldsymbol{J}^\intercal\boldsymbol{r}$. Returning to the general, non-linear case, we have:

$$\nabla f(\boldsymbol{x}) = \sum_{j=1}^{m} r_j(\boldsymbol{x})\nabla r_j(\boldsymbol{x}) = \boldsymbol{J}^\intercal(\boldsymbol{x})\boldsymbol{r}(\boldsymbol{x}) \tag{A.3}$$

$$\nabla^2 f(\boldsymbol{x}) = \boldsymbol{J}^\intercal(\boldsymbol{x})\boldsymbol{J}(\boldsymbol{x}) + \sum_{j=1}^{m} r_j(\boldsymbol{x})\nabla^2 r_j(\boldsymbol{x}) \tag{A.4}$$

The distinctive property of least-squares problems is that given the Jacobian matrix $\boldsymbol{J}$, we can essentially get the Hessian ($\nabla^2 f(\boldsymbol{x})$) for free if it possible

to approximate the r_js by linear functions ($\nabla^2 r_j(\boldsymbol{x})$ are small) or the residuals ($r_j(\boldsymbol{x})$) themselves are small. The Hessian in this case simply becomes

$$\nabla^2 f(\boldsymbol{x}) = \boldsymbol{J}^\intercal(\boldsymbol{x})\boldsymbol{J}(\boldsymbol{x}) \tag{A.5}$$

which is the same as for linear case. The common approximation used here is one of near-linearity of the r_js near the solution so that $\nabla^2 r_j(\boldsymbol{x})$ are small. It is also important to note that A.5 is only valid if the residuals are small. Large residual problems cannot be solved using the quadratic approximation, and consequently, the performance of the algorithms presented here is poor in such cases.

The most intuitive, and simplest technique to find minima in a function is the gradient descendent. Parameter updation is performed by adding the negative of the scaled gradient at each step, i.e.

$$\boldsymbol{x}_{i+1} = \boldsymbol{x}_i - \lambda \nabla f \tag{A.6}$$

Simple gradient descendent suffers from various convergence problems. Logically, we would like to take large steps down the gradient at locations where the gradient is small (the slope is gentle) and conversely, take small steps when the gradient is large, so as not to rattle out of the minima. With the above update rule, we do just the opposite of this. Another issue is that the curvature of the error surface may not be the same in all the directions. For example, if there is a long and narrow valley in the error surface, the component of the gradient in the direction that points along the base of the valley is very small while the component along the valley walls is quite large. This results in motion more in the direction of the walls even though we have to move a long distance along the base and a small distance along the walls. This situation can be improved upon by using curvature as well as gradient information, namely second derivatives. One way to do this id to use Newton's method to solve the equation $\nabla f(\boldsymbol{x}) = 0$. Expanding the gradient of f using Taylor series around the current state $\boldsymbol{x}_0$, we get

$$\nabla f(\boldsymbol{x}) = \nabla f(\boldsymbol{x_0}) + (\boldsymbol{x} - \boldsymbol{x}_0)^\intercal \nabla^2 f(\boldsymbol{x}_0) + o((\boldsymbol{x} - \boldsymbol{x}_0)^2) \tag{A.7}$$

If we neglect the higher order terms (assuming f to be quadratic around x_0), and solve for the minimum $\boldsymbol{x}$ by setting the left hand side of A.7 to 0, we get the update rule for Newton's rule method

$$\boldsymbol{x}_{i+1} = \boldsymbol{x}_i - (\nabla^2 f(\boldsymbol{x}_i))^{-1} \nabla f(\boldsymbol{x}_i) \tag{A.8}$$

where $\boldsymbol{x}_0$ has been replaced by $\boldsymbol{x}_i$ and $\boldsymbol{x}$ by $\boldsymbol{x}_{i+1}$.

Since Newton's method implicitly uses a quadratic assumption on f (arising from the neglect of higher order terms in a Taylor series expansion of f), the Hessian need not be evaluated exactly. Rather the approximation of A.5 can be used. The main advantage of this technique is rapid convergence. However, the

rate of convergence is sensitive to the starting location (or more precisely, the linearity around the starting location).

It can be seen that simple gradient descendent and Gauss-Newton iteration are complementary in the advantages they provide. Levenberg proposed an algorithm based on this observation, whose update is blend of the above mentioned algorithms and is given as

$$\boldsymbol{x}_{i+1} = \boldsymbol{x}_i - (H + \lambda I)^{-1} \nabla f(\boldsymbol{x}_i) \tag{A.9}$$

where H is the Hessian matrix evaluated at $\boldsymbol{x}_i$. This update rule is used as follows. If the error goes down following an update, it implies that our quadratic assumption on $f(\boldsymbol{x})$ is working and we reduce λ (usually by a factor of 10) to reduce the influence of gradient descent. On the other hand, if the error goes up, we would like to follow the gradient more and λ is increased by the same factor. The Levenberg algorithm is thus

1. Do an update as directed by the rule above.

2. Evaluate the error at the new parameter vector.

3. If the error has increased as a result of the update, then retract the step (i.e. reset the weights to their previous values) and increase λ by a factor of 10 or some such significant factor. Then go to (1) and try an update again.

4. If the error has decreased as a result of the update, then accept the step (i.e. keep the weights at their new values) and decrease λ by a factor of 10 or so.

The above algorithm has the disadvantage that if the value of λ is large, the calculated Hessian matrix is not used at all. We can derive some advantage out of the second derivative even in such cases by scaling each component of the gradient according to the curvature. This should result in *larger* movement along the directions where the gradient is *smaller* so that the classic "error valley" problem does not occur any more. This crucial insight was provided by Marquardt. He replaced the identity matrix in A.9 with the diagonal of the Hessian resulting in the Levenberg-Marquardt update rule.

$$\boldsymbol{x}_{i+1} = \boldsymbol{x}_i - (H + \lambda \text{diag}[H])^{-1} \nabla f(\boldsymbol{x}_i) \tag{A.10}$$

Since the Hessian is proportional to the curvature of f, A.10 implies a large step in the direction with low curvature (i.e., an almost flat terrain) and a small step in the direction with high curvature (i.e., a step incline).

It to be noted that while the LM method is in no way optimal but is just a heuristic, it works extremely well in practice. The only flaw is its need for matrix inversion as part of the update. Even though the inverse is usually implemented

using clever pseudo-inverse methods such as singular value decomposition, the cost of the update becomes prohibitive after the model size increases to a few thousand parameters. For moderately sized model (of few hundred parameters) however this method works well.

Appendix B

Coefficient of determination R^2 or r^2

A statistic that is widely used to determine how well a model fits a set of data is the quantity named the *coefficient of determination*. The notation r^2 is usually used for linear, exponential, and power function models, while R^2 is used for other types of models. The formula for R^2 (or r^2) is shown below, where the values of y are from the original set of sample data, $\hat{y}$ denotes values predicted by the model, and $\overline{y}$ is the mean of the original y values.

$$R^2 = 1 - \frac{\sum(y - \hat{y})^2}{\sum(y - \overline{y})^2} \tag{B.1}$$

The following are some key points about the coefficient of determination:

- Values of R^2 are always between 0 and 1.
- If $R^2 = 0$, the model fits the sample data as poorly as it is possible.
- If $R^2 = 1$, the model fits the sample data perfectly.
- In general, better models result in values of R^2 that are closer to 1.

Bibliography

[1] F. Montemurro, F. Russo, and L. Martincich. Dynamic contrast enhanced magnetic resonance imaging in monitoring bone metastases in breast cancer patients receiving bisphosphonates and endocrine therapy. *Acta Radiol.*, 45:71–74, 2004.

[2] T. Tonini, F. Rossi, and P. Claudio. Molecular basis of angiogenesis and cancer. *Oncogene*, 22:6549–6556, 2003.

[3] Ehrmann RL and Knoth M. *J. Natl. Cancer Ins.*, 41:1329–1341, 1968.

[4] J. Folkmann. *New. Engl. J. Med.*, 285:1182–1186, 1971.

[5] R. Brasch and K. Turetschek. MRI characterization of tumors and grading angiogenesis using macromolecular contrast media: status report. *Eur J Radiol*, 34:148–155, 2000.

[6] J. S. Taylor and P. S. Tofts. MR Imaging of Tumor Microcirculation: Promise for the New Millenium. *J. Magn. Reson. Im.*, 10:903–907, 1999.

[7] S. Rehman and G. C. Jayson. Molecular Imaging of Antiangiogenic Agents. *Oncologist*, 10:92–103, 2005.

[8] Timothy P. L. Roberts. Physiologic Measurements by Contrast-Enhanced MR Imaging: Expectations and Limitations. *J. Magn. Reson. Im.*, 7:82–90, 1997.

[9] Min-Ying Su, Jo-Chi Jao, and Orhan Nalcioglu. Measurement of Vascular Volume Fraction and Blood-Tissue Permeability Constant with a Pharmacokinetic Model: Studies in Rat Muscle Tumor with Dynamic Gd-TPDA Enhanced MRI. *Magnet. Reson. Med.*, 32:714–724, 1994.

[10] Pauls S. Toft, Gunnar Brix, David L. Buckley, Jeffrey L. Evelhoch, Elizabeth Henderson, Michaell V. Knopp, Henrik B. W. Larsson, Ting-Yim Lee, Nina A. Mayr, and Geoffreey J. M. Parker. Estimating Kinetic Parameters From Dynamics Contrast-Enanced T_1-Weighted of a Diffusable Tracer: Standardized Quantities and Symbols. *J. Magn. Reson. Im.*, 10:223–232, 1999.

[11] David L. Buckley. Uncertainty in the Analysis of Tracer Kinetics Using Dynamic Contrast-Enhanced T_1-Weighted MRI. *Magnet. Reson. Med.*, 47:601–606, 2002.

[12] Judith U. Harrer, Geoff J.M.Parker, et al. Comparative Study of Methods for Determining Vascular Permeability and Blood Volume in Human Gliomas. *J. Magn. Reson. Im.*, 20:748–757, 2004.

[13] C. Cohen, B. Diu, and F. Laloe. *Mecanique Quantique tome II.* Hermann, 1973.

[14] Z. H. Cho, Joie P. Jones, and Manbir Singh. *Foundations of Medical Imaging.* Wiley, 1993.

[15] Andrè E. Merbach and Èva Toth, editors. *The Chemistry of Contrast Agents in Medical Magnetic Resonance Imaging.* John Wiley & Sons, 2001.

[16] E. Mark Haake, Robert W. Brown, Michael R. Thompson, and Ramesh Venkatesan. *Magnetic Resonance Imaging, Physical Principles and Sequence Design.* Wiley Liss, 1999.

[17] Zhi-Pei Liang and Paul C. Lauterbur. *Principles of Magnetic Resonance Imaging, A Signal Processing Perspective.* IEEE PRESS, 2000.

[18] E. Mark Haake, Robert W. Brown, Michael R. Thompson, and Ramesh Venkatesan. *Magnetic Resonance Imaging, Physical Principles and Sequence Design*, chapter 15 and 20. Wiley Liss, 1999.

[19] Paul T. Callaghan. *Principles of Nuclear Magnetic Resonance Microscopy.* Clarendon Press, 1991.

[20] Pasquina Marzola, Paolo Farace, Laura Calderan, Caterina Crescimanno, Ernesto Lunati, Elena Nicolato, Donatella Benati, Anna Degrassi, Andrea Terron, Jan Klapwijk, Enrico Pesenti, Andrea Sbarbati, and Francesco Osculati. In vivo mapping of fractional plasma volume (FVP) and endothelial transfer coefficient (KPS) in solid tumors using a macromolecular contrast agent: correlation with histology and ultrastructure. *Int. J. Cancer*, 104:462–468, 2003.

[21] Henrik B. W. Larsson, Max Stubgaard, Lars Sondergaard, and Ole Henriksen. In Vivo Quantification of the Unidirectional Influx Constant for Gd-DTPA Diffusion across the Myocardial Capillaries with MR Imaging. *J. Magn. Reson. Im.*, 4:433–440, 1994.

[22] Paul S. Tofts, Gareth J. Barker, et al. Correction of Nonuniformity in Images of the Spine and Optic Nerve from Fixed Receive-Only Surface Coils at 1.5 T. *J. Comput. Assist. Tomo.*, 18(6):997–1003, 1994.

[23] Evan K. Fram, Robert J. Herfkbnens, et al. Rapid Calculation of T1 using Variable Flip Angle Gradient Refocused Imaging. *Magn. Reson. Imaging*, 5:201–208, 1987.

[24] J. A. Brookes, T. W. Redpth, et al. Measurement of spin-lattice relaxation times with FLASH for dynamic MRI of the breast. *Brit. J. Radiol.*, 69:206–214, 1996.

[25] Henry Z. Wang, Stephen J. Riederer, and James N. Lee. Optimizing the Precision in T_1 Relaxation Estimation Using Limited Flip Angle. *Magnet. Reson. Med.*, 5:399–416, 1987.

[26] Geoffrey J.M. Parker, Gareth J. Barker, and Paul S. Tofts. Accurate Multisclice Gradient Echo T_1 Measurement in the Presence of Non-ideal RF Pulse Shape and RF Field Nonuniformity. *Magnet. Reson. Med.*, 45:838–845, 2001.

[27] M. J. Graves. Magnetic resonance angiography. *Brit. J. Radiol.*, 70:6–28, 1997.

[28] Markus Barth and Ewald Moser. Proton NMR Relaxation Times of Human Blood Samples at 1.5 T and Implication for fMRI. *Cell. Mol. Biol.*, 43:783–791, 1997.

[29] Luis Ibanez, Will Schroeder, Lydia Ng, Josh Cates, and the Insight Software Consortium. *The ITK Software Guide*. 2005.

[30] Mark A. Horsfield and Bruno Morgan. Algorithms for Calculation of Kinetic Parameters From T_1-Weighted Dynamic Contrast-Enhanced Magnetic Resonance Imaging. *J. Magn. Reson. Im.*, 20:723729, 2004.